Development of Mobile Photometer for DNA Quantitation Using UV-LED

K. Thamthinthai[1], S. Dangtip[1,2*], S. Senapin[3,4]

[1]Department of Physics, Faculty of Science, Mahidol University, Bangkok 10400, Thailand

[2]NANOTEC Center of Excellence, Faculty of Science, Mahidol University, Bangkok 10400, Thailand

[3]BIOTEC, National Science and Technology, Development Agency, Klong Luang, Pathumthani 12120, Thailand

[4]Centex Shrimp, Faculty of Science, Mahidol University, Bangkok 10400, Thailand

*E-mail: somsak.dan@mahidol.edu

Abstract

Light as electromagnetic wave, when travelling through liquid solution, could perturb and interact with molecules in the solution. Such interaction results in DNA characteristic absorption 260 nm. The absorbance is proportional to DNA concentration through Beer-Lambert law of absorption. This relationship is a common basis of DNA quantification in spectrophotometers. A bulky deuterium lamp or halogen lamp is commonly used as 260-nm light source. Their use has limited a mobility of spectrophotometer. UV-LED is an alternative light source with lighter weight and more compact in size. In this work, we have developed 260-nm LED and a photo-diode as a compact and mobile photometer. At present, the development is still in its early stage. Some experimental results of DNA quantification are reported in this conference.

Keywords: Mobile photometer, DNA quantitation, UV-LED

Introduction

Light when travelling through a liquid solution, it excites molecules in that solution from ground to higher excited state. Some light is absorbed during exciting process. Structure of molecules in solution determine wavelength region of light absorption. DNA has four nucleotides as its basic unit which their structures are aromatic rings. This ring structure results in $n \rightarrow \pi^*$ and $\pi \rightarrow \pi^*$ transitions which produce light absorption normally in the UV region, wavelength around 200 nm – 300 nm. In general DNA solution, peak maximum occurs at 260 nm [1]. Absorbance at 260 nm is thus directly proportional to concentration of DNA by Beer-Lambert law of absorption which used for DNA quantification in spectrophotometer.

In theoretical quantitation of DNA, 1 absorbance unit refers to dsDNA of 50 ug/mL concentration [2].

In general spectrometer, their components are bulky and complex. In order to minimize its size and weight [3], Deuterium and Halogen light sources are replaced by smaller UV-LED. Photo-diode is used as light detector. With these two components, photometer are compact and mobile.

In this paper, development of mobile UV-LED photometer for DNA quantification is reported.

Materials and Methods

Two LEDs and photodiodes are used as light source and light detector, respectively. LED is made of aluminium gallium nitride (AlGaN). It generates light in UV region. Their peak maximum wavelengths are at 260 nm and 280 nm. On top of the LEDs case, there

be a hemispherical lens attached for light collimation. LEDs are connected with LED driver IC (CL520 from Supertex inc.) to control forward current at typically 20mA. Total light power is about 0.5 mW for each LED.

Photodiodes (SG01M-lens from SGLUX) are used for light detection after DNA solution. Photodiode semiconductor materials is made from silicon carbide (SiC). A collimating lens on the top helps focusing light for better photodiode's efficiency. It is near-perfect visible blindness and low dark current. It is connected in photovoltaic mode (forward biasing) for accurate current signal.

Operational amplifier (OP2336, Texas instrument) is used to convert current signal from photodiode into voltage signal and amplify before sending to voltmeter. Next, an output voltage is measured by Tektronix oscilloscope (TDS2012C).

A quartz cuvette of 1-cm light path length is utilized as a container for DNA solution.

DNA solution preparation process: original dsDNA solution was diluted in series into four concentrations. Each concentration was further separated into two groups. The first group was measured for its absorbance at 260 and 280 nm by an equipment under this study; while the second group by a commercial spectrophotometer. In both cases, water is used as reference solution. The absorbance at 260 nm (A_{260}) by a commercial spectrophotometer is converted to concentrations by [2]

$$C\left(\frac{ug}{mL}\right) = \frac{A_{260}}{0.020} \qquad (1)$$

While, the output voltage signal from the equipment using 260- and 280-nm LED under this study is converted into absorbance as A_{260} and A_{280}, respectively, by [3]

$$A_x = -\log\left(\frac{V_x}{V_{ref}}\right) \qquad (2)$$

Then, one can establish a calibration curve for a photometer under this study from absorbance in DNA solution to concentration by correlating through linear regression between the two data sets; one from the photometer under this study and the other from a commercial spectrophotometer.

Results and Discussion

Table 1 shows concentrations of dsDNA and their absorbance values (A_{260} and A_{280}) measured from a commercial spectrophotometer. Solution#1 is water (no DNA) to set A_{260} to 0.000. A_{260} of solution #2 to #5 can be clearly observed and are linearly proportional to DNA concentration. Next, DNA concentration was determined by calculating from Equation (1).

Table 1 Concentration of DNA converting from absorbance

No.	A_{260}	A_{280}	A_{260}/A_{280}	Concentration (ug/mL)
1	0.000	0.000	-	0.00
2	0.230	0.123	1.890	11.5
3	0.584	0.307	1.902	29.2
4	0.734	0.382	1.921	36.7
5	0.927	0.479	1.923	46.4

Table 2 summarizes output voltage obtained from DNA solutions at various concentration. These values were obtained from two different light LEDs; 260- and 280-nm as labeled as subscript and as shown in Column 2 and 4, respectively. These voltages were converted to absorbance (Equation (2)) and were shown in column 3 and 5 in Table 2.

Table 2 Average voltage and absorbance from photometer.

No.	V_{260}	A_{260}	V_{280}	A_{280}
1	2.728	0.000	3.773	0.000
2	2.550	0.230	3.775	0.000
3	1.808	0.584	1.898	0.299
4	1.635	0.734	1.633	0.365
5	1.388	0.927	1.125	0.527

Absorbance data from a commercial spectrophotometer (cf Table 1) are plotted (upper line in Figure 1) along with those from a photometer under this study (cf Table 2 and shown as lower line). It can be clearly seen that both equipment has their linear response over the measuring range.
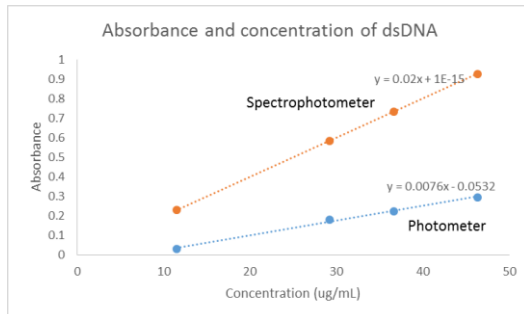

Figure 1 Absorbance as a function of DNA concentration from a commercial spectrophotometer and a photometer built in this study.

Then a linear relation between the absorbance from our equipment to the commercial one can now be established, i.e. calibration curve. Figure 2 shows the relation between the two equipment for A_{260} case and Figure 3 for A_{280} case. The linear regression between the two sets are:

$$A_{260}: \quad A_{commercial} = 2.625 * A_{pho} + 0.142 \tag{3}$$

$$A_{260}: \quad A_{commercial} = 0.681 * A_{pho} + 0.120 \tag{4}$$

Table 3 compares absorbance results between the commercial spectrophotometer and the photometer built for this study.

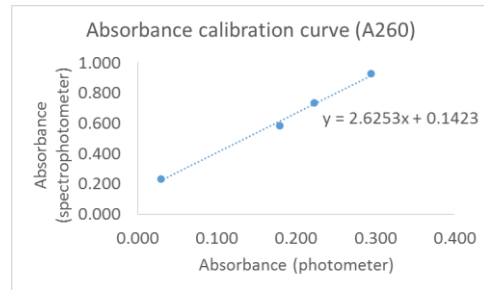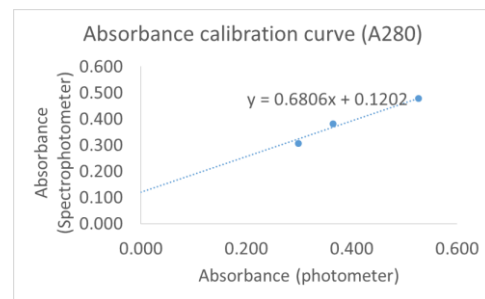**Figure 2** Absorbance (A_{260}) calibration curve.

Figure 3 Absorbance (A_{280}) calibration curve.

Table 3 Calibrated absorbance (A_{260} and A_{280}) from photometer (this study) and from spectrophotometer (commercial).

No.	A_{260} (com)	A_{260}	A_{280} (com)	A_{280} P
1	0.000	0.000	0.000	0.000
2	0.217	0.230	0.000	0.123
3	0.612	0.584	0.323	0.307
4	0.727	0.734	0.368	0.382
5	0.915	0.927	0.479	0.479

Conclusions

A mobile photometer has been built at relative low cost and tested against the commercial and more bulky spectrophotometer. This photometer will be added with more functions during the course of this study. It is foreseen to be utilized in the field.

References

[1] Biophysical Chemistry, Part 2**: Techniques for the Study of Biological Structure and Function**, Cantor and Paul R. Schimmel, W. H. Freeman and Company; 1st edition (April 15, 1980).

[2] Sean, R. G. 1994. **"Quantitation of DNA and RNA with Absorption and Fluorescence Spectroscopy**". Current protocols in Molecular Biology. A.3D, 1-8.

[3] Stewart, J. Tavener and Jane E. Thomas-Oates. September 2007 "Build your own spectrophotometer". **Education in chemistry.** 151 -154.

Size Controlling of Nanoparticle for DNA Detection

T. Wangkam[1*], K. Techasuksakul[1], S. Kanjai[1], K. Nawattanapaiboon[2], and T. Srikhirin[2]

[1]Department of Industrial Physics and Medical Instrumentation, Faculty of Applied Science, King Mongkut's University of Technology North Bangkok, 1518 Pracharat 1 Road, Bangsue, Bangkok 10800 Thailand

[2]Materials science and Engineering programme, Faculty of Science, Mahidol University, Rama VI Road, Ratchathewi District, Bangkok 10400 Thailand

*E-mail:thidarat.w@sci.kmutnb.ac.th

Abstract

Recently, DNA detection have been designed for higher precisely detection. One of DNA sensor is the DNA tagging with nanoparticles. It is widely used to apply in a variety of target including nucleic acids, small molecule and protein. This work would show the possibility of applying the nanoparticles in DNA hybridization detection. The characteristics of the nanoparticles were studied by transmission electron microscopy (TEM) and Ultraviolet spectroscopy in real serum solution by using a simple optical technique. The results was shown about the key parameters for size changing in nanoparticles and correlation to the capability of DNA detection. Some parameters such as time for seed growth, pH value and acids reagents were proved that there are effect on the size of nanoparticles.

Keywords: Gold nanorods, Nanoparticle, Size controlling

Introduction

The prevalence of new and current diseases is rising continuously. A high sensitivity and rapid detection are main concern for the development, especially in clinical diagnostic. Small molecules were detected by highly sensitive method. Gold nanorods (GNRs) is a one of fruitful substance which can be designed on each applications. It has been used in a broad range of biological, industry, chemical and biomedical applications due to their brilliant optical properties. In nanotechnology, nanorods are one morphology of nanoscale objects. Each of their dimensions range from 1–100 nm. They may be synthesized from gold, silver and other metals. Aspect ratios are 3-5. Nanorods are produced by direct chemical synthesis. A combination of ligands can be bond to different facets of the nanorod with different strengths. This allows different faces of the nanorod to grow at different rates and different aspect ratio.

Because the reflectivity of the rods can be changed by changing their orientation with an applied electric field. The nanorods is wikdely use for microelectromechanical systems (MEMS) also function as medical diagnostic agents, be able to absorb in the near IR, and generate heat when excited with IR light. These properties have led to the use of nanorods as sensitive substance for our work. This work, we study the major parameter for adjusting of nanoparticles sizes which reach to multiplexed detection in medical application further.

Materials and Methods
Synthesis of gold nanorods

Seed Solution: For the preparation of the seeds, Gold (III) chloride trihydrate (HAuCl$_4$•3H$_2$O) was used.

To 5 ml of 0.20 M CTAB, 0.1ml of gold stock solution (0.5 mM). While stirring, 0.6 ml of 0.01 M ice cold $NaBH_4$ was added, and stirring continued for 2 min. The solution turned light-brown immediately after addition of $NaBH_4$ indicating particle formation. The seed solution was left undisturbed for 2 h at room temperature before usage to allow excess borohydride to be completely decomposed [2,3].

Results and Discussion

Effect of $AgNO_3$

Growth of gold nanorods: For the growth solution, 15 ml of 0.20 M CTAB was mixed with 0.6 ml gold stock solution (0.001 mM). Subsequently, (60, 100, 150, 180 µl) of 0.02 M $AgNO_3$ was added, followed by 210 µl of 0.078 mM ascorbic acid (AA); the solution quickly turned from dark yellow to clear and colourless. To this colourless solution, 0.1 ml of seed solution was added to each growth solution at about 30.5 °C. The color of the GNRs solutions was gradually changed within 30 min. The mixture was kept at 30.5 °C without being disturbed for 24 h. to allow the gold nanorods to grow fully [2,3]. Purification was done by centrifugating twice at 10,000 rpm for 10 min.
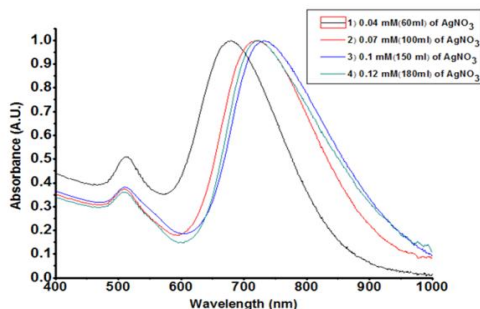

Figure 1 UV–vis absorption spectra of the AuNRs

UV–vis absorption spectra of the AuNRs solutions synthesized starting from different $AgNO_3$ concentrations. As can be seen, initially increasing the concentration of $AgNO_3$ solution from 0.04, 0.07 and 0.1 mM, we induce red shift of the LSP absorption peak from 679 to 732 nm. Further increase of the $AgNO_3$ concentration to 0.12 mM leads to blue shift of the LSP absorption peak to 728 nm.

In the case of addition of AA (Figure 2), is reached for the concentration that maximizes the precursor solution peak at 679, 718 and 732. As a function of pH for binding The graph of the pH, prepared from pH 3.8, 3.2, 3 shows a λ_{max}(nm) at about 826, 831, 843nm by used to $AgNo_3$ concentration 0.04, 0.07, 0.1 mM, respectively.

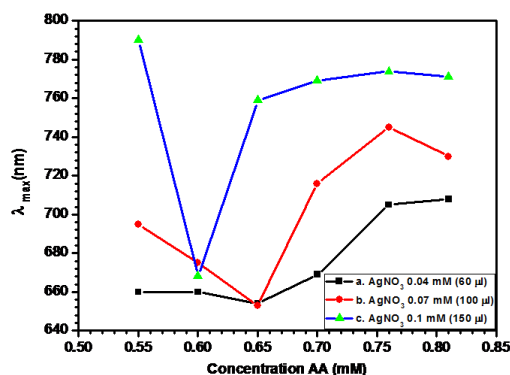**Figure 2** Effect of AA concentration

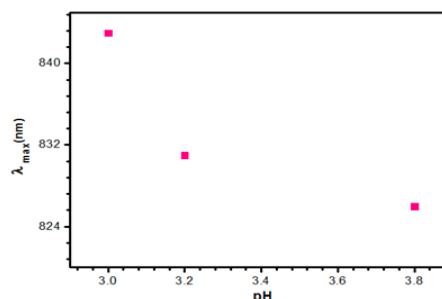**Figure 3** The λ_{max}(nm) shift as a function of pH for binding of pH with different concentrations.

The graph of the pH (Figure 3), prepared from pH 3.8, shows a λ_{max}(nm) at about 826 nm by used to $AgNo_3$ concentration 0.04 mM. The increase of the HCl results in the increase from the original at 147 nm. The increases pH 3.8, shows a λmax(nm) at about 826 nm by used to $AgNO_3$ concentration 0.07 mM. The increase of the HCl results in the increase from the original at 113 nm. The increases pH 3, shows a λmax(nm) at about 843 nm by used to

$AgNO_3$ concentration 0.1 mM. The increase of the HCl results in the increase from the original at 111 nm.

Conclusions

In summary, gold nanorods were prepared with a single step photochemical method at different silver nitrate ($AgNO_3$), ascorbic acid (AA) and Hydrochloric acid (HCl) concentrations. Experimentally we showed that the gold nanorods aspect ratio and its concentration can be controlled by appropriately adjusting the concentration of silver nitrate (AgNO3), ascorbic acid (AA) solution. In synthesis of gold nanorods at $AgNO_3$ concentrations 0.1 mM, shows a peak of absorption band centered at about 700 nm, 0.55 mM AA solution and 1mM HCl concentrations is optimum condition for study in medical application further.

Acknowledgments

References

[1] A. Chompoosor, 2013. "Gold Nanostructures: Synthesis and Applications for Cancer Therapy". **KKU Science Journal.** Volume 41 Number 4, 859-872.

[2] Jie Cao, Ewan K. Galbraith, Tong Sun, and Kenneth T.V. Grattan, B. B. 2011. "Effective surface modification of gold nanorods for localized surface plasmon resonance-based biosensors". **Sensors and Actuators B: Chemical**. 169: 360–367

[3] E.S. Kooij, W. Ahmed, C. Hellenthal, H.J.W. Zandvliet, B. Poelsema, 2012. "From nanorods to nanostars: Tuning the optical properties of gold nanoparticles". **Colloids and Surfaces A: Physicochemical and Engineering Aspects**. 413 : 231–238.

[4] Babak Nikoobakht and Mostafa A. El-Sayed. 2003."Preparation and Growth Mechanism of Gold Nanorods (NRs) Using Seed-Mediated Growth Method". **Chemistry of Materials**. 15: 1957-1962.

[5] Setareh Monshi Toussi, Marco Zanella, Gaser Nagah Abdelrasoul, Athanassia Athanassiou, Francesca Pignatelli, 2015. "Twofold role of Hexadecyltrimethylammonium Bromide in photochemical synthesis of gold nanorods" **Journal of Photochemistry and Photobiology A:Chemistry.** Volume number 311: 76–84.

[6] A.R.M. Nabiul Afrooz, Sean T. Sivalapalan, Catherine J. Murphy, Saber M. Hussain, John J. Schlager, Navid B. Saleh, 2013. "Spheres vs. rods: The shape of gold nanoparticles influences aggregation and deposition behavior" **Chemosphere** . 91: 93–98.

[7] Kristina L. Tran. 2010. "Synthesis, Characterization, and Self-Assembly of Gold Nanorods and Nanoprisms". **Scholar Commons**.

[8] Mohammadi-Motlagh, H.R., Mostafaie, A., and Mansouri, K. 2011. "Anticancer and anti-inflammatory activities of shallot (Allium ascalonicum) extract". **Arch Med Sci**. 7: 38-44.

[9] Calixto, J.B., Campos, M.M., Otuki, M.F., and Santos, A.R. 2004. "Antiinflammatory compounds of plant origin. Part II. modulation of proinflammatory cytokines, chemokines and adhesion molecules". **Planta Med**. 70: 93-103.

[10] Polyon, C. 2010. "Magnetic Detectors". **Proceeding of Ubon Ratchthani University Conference**. pp. 238-245.

Colossal Dielectric Properties of (Sc+Nb) Co-Doped TiO$_2$ Ceramics

N. Thanamoon and P. Thongbai*

Integrated Nanotechnology Research Center (INRC), Department of Physics, Faculty of Science,

Khon Kaen University, Khon Kaen 40002, Thailand

* Email: pthongbai@kku.ac.th

ABSTRACT

The giant dielectric properties of (Sc+Nb) co—doped TiO$_2$ (SNTO) ceramics with different doping concentrations were investigated. Phase composition and microstructure were characterized by X-ray diffraction and scanning electron microscope, respectively. The mean grain size decreased as co-doping concentration increased. Giant ε' value of $\approx 9.2 \times 10^5$ with slight temperature dependence over a wide range from room temperature to 200 ^{o}C was successfully achieved in SNTO ceramics. The dielectric relaxation behavior was observed with activation energy of about 0.182 eV. The giant ε' response over a broad temperature range in SNTO ceramics was due to the polarization of highly localized electrons in large defect—dipole clusters and internal barrier layer capacitor effect.

Keywords: TiO$_2$, Giant permittivity, Scanning electron microscope, Loss tangent, Dielectric relaxation.

Introduction

Recently, excellent dielectric properties in a (In+Nb) co—doped rutile—TiO$_2$ (IN—T) ceramic system were reported   [1]. Very low $\tan\delta \approx 0.02$-0.05 and giant dielectric value ($\varepsilon' \sim 10^4$) were observed in (In$_{0.5}$Nb$_{0.5}$)$_x$Ti$_{1-x}$O$_2$ ceramics. Furthermore, ε' was frequency independent over the range of 10^2—10^6 Hz and was slightly dependent of temperature over a wide range. These interesting dielectric properties were caused by the formation of large defect—dipole clusters containing highly localized electrons. Further investigation reported that the internal barrier layer capacitor (IBLC) mechanism has also an effect on the giant dielectric properties of TiO$_2$-based ceramics [2, 3]. According to the first mechanism, defect clusters are produced by the complex stoichiometry of (In$_x^{3+}$Nb$_x^{5+}$Ti$_x^{3+}$)Ti$_{1-3x}^{4+}$O$_{2-x/2}$. The electrons created by Nb^{5+} doping ions are contained in defect clusters produced by In^{3+} doping ions [4]. Electrons are

delocalized when In^{3+} dopant was not introduced, leading to high DC conductivity and $\tan\delta$ values. Now, other co-doping ions used to substitute in TiO$_2$ for enhancing dielectric response have been reported [5-9]. It was reported that difference in ionic radii between co-doping ions and the host Ti^{4+} has a great effect on the primary mechanism contributing to the overall dielectric properties [5, 6]. The surface barrier layer capacitor (SBLC) effect was dominated by co-doping with (Ga+Nb) ions. To the best our knowledge, there is no report on the enhanced dielectric response in (Sc+Nb) co-doped rutile TiO$_2$ (SNTO).

In this paper, we therefore report the dielectric properties of (Sc+Nb) co-doped rutile TiO$_2$. We found that the ε' value of TiO$_2$ was extremely enhanced by co-doping with Sc^{3+} and Nb^{5+} ions. The origin(s) of the giant dielectric response in SNTO was discussed.

Materials and Methods

$Sc_{0.005}Nb_{0.005}Ti_{0.99}O_2$, $Sc_{0.010}Nb_{0.010}Ti_{0.98}O_2$, $Sc_{0.010}Nb_{0.010}Ti_{0.98}O_2$, $Sc_{0.010}Nb_{0.020}Ti_{0.97}$ O_2 ceramics (abbreviated as SNTO-1, SNTO-2, SNTO-3, and SNTO-4 samples, respectively) were prepared using a solid state reaction method. TiO_2, Nb_2O_5, and Sc_2O_3 were used as the starting raw materials. First, a stoichiometric mixture of the starting materials was ball—milled in ethanol for 24 h using ZrO_2 balls. Second, the mixed powders were ground. Then, the obtained SNTO powders were pressed into pellets of 9.5 mm in diameter and ≈1.2 mm in thickness at ≈200 MPa. Finally, these pellets were sintered at 1400 $^\circ$C for 5 h.

X—ray diffraction (XRD; Bruker, D 2phaser) was used to characterize the phase composition and crystal structures of the sintered ceramics. Scanning electron microscopy (SEM) (SEC, SNE4500M) was used to reveal the microstructure of the sintered ceramics. Au was sputtered onto pellet faces at using a Polaron SC500 sputter coating unit (Sussex, UK). The dielectric properties of the sintered ceramic samples were measured using KEYSIGHT E4990A Impedance Analyzer over the frequency and temperature ranges of 10^2—10^6 Hz and -70—220 $^\circ$C, respectively.

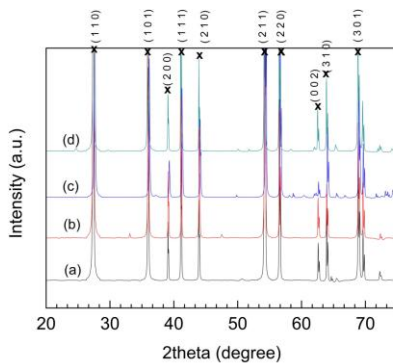## Results and Discussion

Figure 1 XRD patterns of SNTO-1(a), SNTO-2(b), SNTO-3(c) and SNTO-4(d) samples.

Figure 1 shows the XRD patterns of all sintered SNTO ceramics with different doping concentrations. The main phase of rutile—TiO_2 (JCPDS 21—1276) is observed in the samples. The diffraction peaks in these XRD patterns are perfectly indexed as a tetragonal structure. Lattice parameters were calculated from the diffraction peaks and found to be a=4.599 Å and c=2.965 Å, a=4.606 Å and c=2.970Å, a=4.513 Å and c=2.906Å, and a=4.509 Å and c=2.902 Å for the SNTO-1, SNTO-2, SNTO-3, and SNTO-4 samples, respectively. The a and c values of all the samples were nearly the same as the sample in values for rutile—TiO_2 (JCPDS 21—1276) with a=4.593 Å and c=2.959 Å.
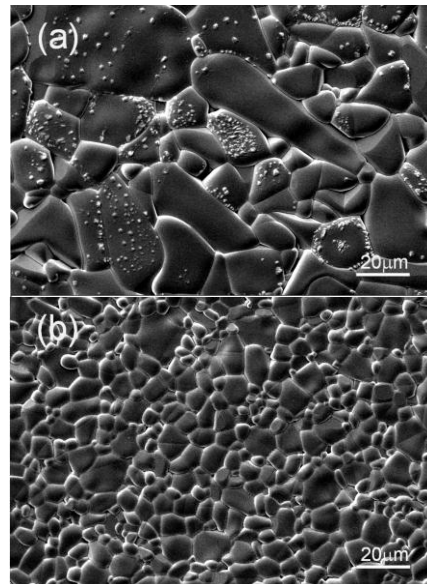

Figure 2 SEM micrographs of SNTO-1 (a) and SNTO-4 (b) samples.

Figures 2(a) and (b) reveal the microstructures of the SNTO-1 and SNTO-4 samples, respectively. The grain size of SNTO ceramics decreased with increasing co—dopant concentration. This is similar to that observed in (In+Nb) co-doped TiO_2 ceramics [10]. The decrease in the grain size is likely due to the solute drag effect [11]. The rate of grain growth in TiO_2 polycrystalline ceramics was inhibited by Sc^{3+} and Nb^{5+}.
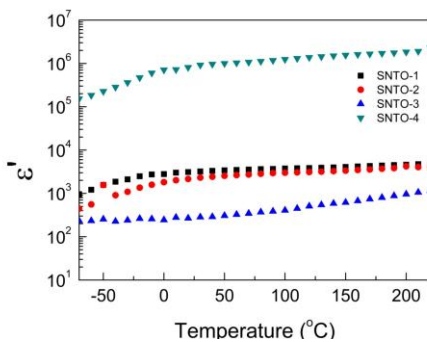
Figure 3 Temperature dependence of ε' at 1 kHz for the (Sc+Nb) co-doped TiO_2 ceramics.
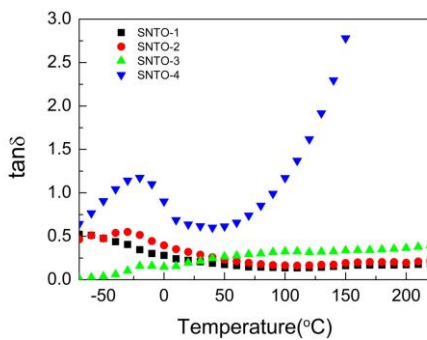

Figure 4 Temperature dependence of $\tan\delta$ at 1 kHz for the (Sc+Nb) co-doped TiO_2 ceramics.

Figure 3 demonstrates the temperature dependence of ε' at 1 kHz for the SNTO ceramics. The effect of co-doping concentration on the dielectric response in SNTO ceramics is clearly observed, especially for the SNTO-4 sample. The ε' values at 30 ^{o}C and 1 kHz for the SNTO-1, SNTO-2, SNTO-3, and SNTO-4 samples are of about 3210, 2311, 284, and 919087, respectively. The extremely enhanced ε' value of the SNTO-4 sample is due to a high doping concentration of Nb^{5+}. This ε' value is much higher than those of other co-doped TiO_2-based materials [1, 3, 5-7, 9, 10]. ε' at 1 kHz is nearly independent on temperature from room temperature to 220 ^{o}C. In a low temperature rage, ε' decreased rapidly, which is attributed to the dielectric relaxation phenomena in SNTO ceramics [12]. The temperature dependence of $\tan\delta$ at 1 kHz for the SNTO ceramics is illustrated in

Figure 4 shows the $\tan\delta$ values at 30 ^{o}C and 1 kHz for the SNTO-1, SNTO-2, SNTO-3, and SNTO-4 samples are of about 0.207, 0.288, 0.214, and 0.617, respectively. High $\tan\delta$ value of the SNTO-4 sample is well consistent with its high ε' value. $\tan\delta$ peak of the SNTO sample is observed in a low-temperature range. This may be caused by the dielectric relaxation process.

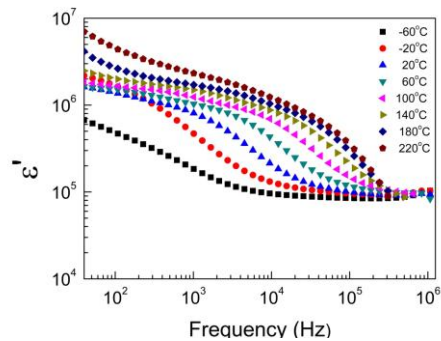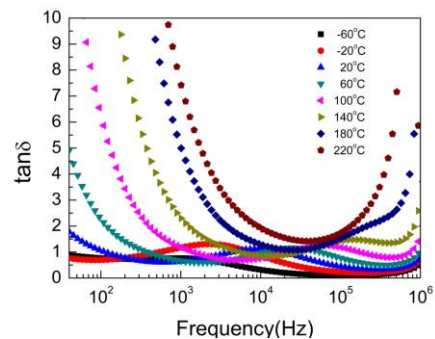**Figure 5** Frequency dependence of ε' for the SNTO-4 sample.

Figure 6 Frequency dependence of $\tan\delta$ for the SNTO-4 sample.

To further characterize the dielectric relaxation phenomena in the SNTO-4 sample, the temperature dependence of dielectric properties were measured at different frequencies, as shown in Figures 5 and 6. The step-like decrease in ε' shifts to high frequencies as the temperature increased. The apparent $\tan\delta$ peak also moves to high frequencies. These clearly indicate to the thermally activated dielectric relaxation process in the SNTO-4 sample [13]. High $\tan\delta$ value

in a low frequency range is attributed to the DC conduction in the bulk ceramic. Such a high $\tan\delta$ value is dominated as the temperature increased.

The total energy loss in dielectric materials is generally the sum of energy loss owing to the DC conductivity and dielectric relaxation process [12]. This is expressed as,

$$\tan\delta = \frac{\omega^2\varepsilon_0\tau(\varepsilon_s' - \varepsilon_\infty') + (1 + \omega^2\tau^2)\sigma_{dc}}{\omega\varepsilon_0(\varepsilon_s' + \varepsilon_\infty'\omega^2\tau^2)} \qquad (1)$$

where ε_s' and ε_∞' are the low- and high-frequency limits of dielectric permittivity, respectively. σ_{dc} is DC conductivity, τ is relaxation time, and ε_0 is permittivity of free space. In a low frequency range, $\omega\tau \ll 1$, Equation (1) can be reduced to be

$$\tan\delta \approx \frac{\sigma_{dc}}{\omega\varepsilon_0\varepsilon_s'} \qquad (2)$$

High $\tan\delta$ is primarily due to the high value of σ_{dc}.

The temperature dependence of the frequency at which the $\tan\delta$ peak occurred (f_{max}) [Fig. 6] follows the Arrhenius equation:

$$f_{max} = f_0 \exp(-E_a / k_B T) \qquad (3)$$

where f_0 is the pre—factor, E_a is the activation energy required for the relaxation process, k_B is the Boltzmann constant, and T is absolute temperature.
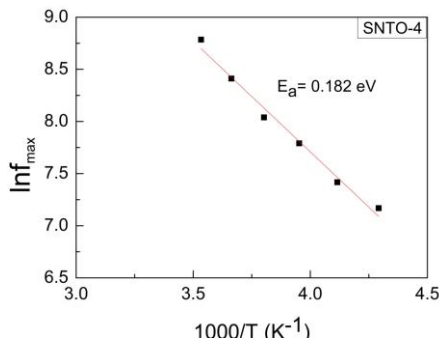

Figure 7 Arrhenius plot of the f_{max} for the SNTO-4 sample.

Figure 7 shows a good linear fit. This result indicates a non—polaron type relaxation due to a hopping motion of localized carriers. The activation energy can be calculated and found to be 0.182 eV. By considering the value of activation energy, the observed dielectric relaxation might be associated with grain boundary response as observed in (In+Nb) co-doped TiO$_2$ ceramics prepared by a spark plasma sintering [14]. Thus, the IBLC effect may contribute to the observed extremely high ε' value in a low-frequency range.

As shown in Figure 5, at -60 $^\circ$C, the ε' value in a relatively high-frequency range is still too large of about 10^5. This indicates to the intrinsic effect in the bulk ceramics. According to the first report of the excellent dielectric properties of (In+Nb) co—doped TiO$_2$ ceramics, the origin of this observation was caused by the existence of local special defect—dipole clusters in the rutile structure [1]. Doping Nb^{5+} into TiO$_2$ produced free electrons and accompanied with reduction of Ti^{4+} to Ti^{3+}, following the relation $2TiO_2 + Nb_2O_5 \xrightarrow{4TiO_2} 2Ti'_{Ti} + 2Nb^{\bullet}_{Ti} + 8O_O + 1/2O_2$ and $Ti^{4+} + e \rightarrow Ti'^{3+}$. This is expected to occur in the SNTO ceramics. On the other hand, doping TiO$_2$ with Sc^{3+} required oxygen vacancies for charge compensation following the relation $Sc_2O_3 \xrightarrow{2TiO_2} 2Sc'_{Ti} + V^{\bullet\bullet}_O + 3O_O$. It is possible that when triangular shaped $Sc_2^{3+}V_O^{\bullet\bullet}Ti^{3+}$ and diamond shaped $Nb_2^{5+}Ti^{3+}A_{Ti}$ (A=Sc^{3+}, Ti^{3+}, or Ti^{4+}) intrinsic defect complexes overlapped, high ε' and low $\tan\delta$ can be accomplished [1]. This is responsible for the observed frequency—independent giant ε' value in co—doped TiO$_2$ ceramics, ranging from 10^2 to 10^6 Hz. Accordingly, it is reasonable to suggest that the high—frequency ε' plateau observed in the current study likely originated from the dielectric response of the intrinsic defect clusters. The low—frequency plateau of ε' is likely related to an extrinsic effect, at which an interfacial polarization of delocalized charges can be produced at grain boundaries, i.e., IBLC effect [1, 15]. Therefore, both of the electron pinned-defect dipoles and IBLC effect have remarkable influences on the giant dielectric response in the SNTO ceramics.

Conclusions

In conclusion, the giant dielectric properties of SNTO ceramics were successfully obtained. The main phase of rutile-TiO_2 was detected in all the samples with different doping concentrations. The grain size decreased with increasing co-doping concentration. The extremely high ε' value of $\approx 9.2 \times 10^5$ with slight temperature dependence over a wide range from room temperature to 200 ^{o}C was successfully achieved. The thermally activated dielectric relaxation was also studied. The activation energy of about 0.182 eV might be due to the grain boundary response. The giant ε' response over a broad temperature range in SNTO ceramics was attributed to the electron pinned defect−dipole clusters and IBLC effect.

Acknowledgments

References

[1] W. Hu, Y. Liu, R.L. Withers, T.J. Frankcombe, L. Norén, A. Snashall, M. Kitchin, P. Smith, B. Gong, H. Chen, J. Schiemer, F. Brink, J. Wong-Leung, Nat. Mater., 12 (2013) 821-826.

[2] X.-g. Zhao, P. Liu, Y.-C. Song, A.-p. Zhang, X.-m. Chen, J.-p. Zhou, Phys. Chem. Chem. Phys., 17 (2015) 23132-23139.

[3] Y. Song, X. Wang, Y. Sui, Z. Liu, Y. Zhang, H. Zhan, B. Song, Z. Liu, Z. Lv, L. Tao, J. Tang, Scientific Reports, 6 (2016) 21478.

[4] C.C. Homes, T. Vogt, Nat. Mater., 12 (2013) 782-783.

[5] W. Dong, W. Hu, A. Berlie, K. Lau, H. Chen, R.L. Withers, Y. Liu, ACS Applied Materials & Interfaces, 7 (2015) 25321-25325.

[6] W. Hu, K. Lau, Y. Liu, R.L. Withers, H. Chen, L. Fu, B. Gong, W. Hutchison, Chem. Mater., 27 (2015) 4934-4942.

[7] Z. Li, J. Wu, W. Wu, Journal of Materials Chemistry C, 3 (2015) 9206-9216.

[8] W. Tuichai, P. Srepusharawoot, E. Swatsitang, S. Danwittayakul, P. Thongbai, Microelectron. Eng., 146 (2015) 32-37.

[9] X. Cheng, Z. Li, J. Wu, Journal of Materials Chemistry A, 3 (2015) 5805-5810.

[10] W. Tuichai, S. Danwittayakul, S. Maensiri, P. Thongbai, RSC Advances, 6 (2016) 5582-5589.

[11] M.N. Rahaman, Ceramic processing and sintering, 2nd ed., M. Dekker, New York, 2003.

[12] K.-C. Kao, Dielectric phenomena in solids : with emphasis on physical concepts of electronic processes, Academic Press, Amsterdam ; Boston, 2004.

[13] J. Wu, C.-W. Nan, Y. Lin, Y. Deng, Phys. Rev. Lett., 89 (2002) 217601.

[14] H. Han, P. Dufour, S. Mhin, J.H. Ryu, C. Tenailleau, S. Guillemet-Fritsch, Phys. Chem. Chem. Phys., 17 (2015) 16864-16875.

[15] T.-T. Fang, C.P. Liu, Chem. Mater., 17 (2005) 5167-5171.

A Survey of ^{226}Ra Level in Water Supply of Amphoe Muang Khon Kaen

V. Atyotha[*]

Department of Applied Physics, Faculty of Engineering, Rajamangala University of Technology Isan, Khon Kaen Campus, Khon Khaen, 40000, Thailand

*E-mail: corresponding: v_atyotha@hotmail.com

Abstract

The ^{226}Ra level in 111 water supply samples of Amphoe Muang Khon Kaen were determined by measuring ^{226}Ra via Mn-fiber using gamma spectrometry. The average of ^{226}Ra was found to be 0.038 Bq/l, range 0 – 0.13 Bq/l. The average risk of Annual Equivalent Dose was found to be 0.023 mSv/ y, range 0 – 0.079 mSv/y. The results were compared to the standard value of the US Environmental Protection Agency (less than 0.11 Bq/l) and Annual Equivalent Dose (less than 0.1 mSv/y).

Keywords: ^{226}Ra, Gamma spectrometry, Water supply, Khon Kaen

Introduction

^{226}Ra is a radioactive that can accumulate in the environment, such as rocks, soil, water, plants and food [1]. However if radioactive is accumulated in the human body in high level, it will affect your health. When people drink water containing ^{226}Ra dissolved in a high volume, can be a cause of cancer in various organs such as the lungs, liver, kidneys and endocrine organs [2, 3]. The researchers were aware of the problems in this regard, so we have measured the amount of ^{226}Ra in drinking water that people use on a regular basis. We choose to study water samples from villages in Research areas in order to measure the safety and the risks that affect the health of people in the study area.

Materials and Methods

The 111 samples of water supply were packaged in 10 liter gallons (Before packing, the water must be opened 5-10 minutes). To trap radium in water samples, they were traped in filter which made from acrylic fiber coated with Potassium permanganate (Mn-fiber). Packaging Mn-fiber filtered in a sealed plastic jar. The jar containing Mn-fiber was measured by gamma spectrometry for 20 hr/sample. Determination of ^{226}Ra in water samples was taken by the peak area from gamma spectrometry. ^{226}Ra is calculated from Equation (1)

$$A_{sample} = \left(\frac{N_{sample}}{(V)(P)(Eff)} \right) \pm \left(\frac{\sigma_{Nsample}}{(V)(P)(Eff)} \right) \quad (1)$$

N_{std} = count rate of standard (cpm)

σ_{Nstd} = error of N_{std}

N_B = count rate of blank (cpm)

σ_{N_B} = error of N_B

N_{sample} = count rate of sample (cpm)

$\sigma_{Nsample}$ = error of N_{sample}

A_{std} = activity of standard (dpm)

A_{sample} = activity of sample (dpm)

V = volume of water (L)

Eff = Efficiency of Probe at 186.2 keV of ^{226}Ra

P = The proportion of gamma radiation at 186.2 keV of ^{226}Ra = 4%

The amount of radiation received per year from drinking contaminated water supply caused by the [226]Ra (Annual Equivalent Dose, AED) was calculated. To assess the radiation from Equation 2 [4]

$$AED = A \times W \times Dose\ factor$$

AED = Radiation received per year (mSv/y)

A = activity of [226]Ra in water (Bq/l)

W = Water consumption per year in men to drink at least two liters a year, so one would have to drink at least 730 liters.

Results and Discussion

[226]Ra and Annual Equivalent Dose in water supply in 10 interesting regions that has an average of [226]Ra higher than other regions at Amphoe Muang Khon Kaen are shown in Table 1.

Table 1 [226]Ra and AED in water supply

Research areas	[226]Ra (Bq/L)	AED (mSv/y)
1. Ban Gudnang Tui Tambom Bantoom	0.13	0.079
2. Ban Khamhai School Tambon Banped	0.115	0.070
3. Banbenggae Tambon Nonton	0.114	0.069
4. Ruenjit Road Tambon Naimeuang	0.0109	0.064
5. Ban Bengniam Tambon Banbengniam	0.0105	0.063
6. Ban Nhongkha Tambon Nonton	0.097	0.059
7. Ban Nongkuay Tambon Thaphra	0.093	0.056
8. Ban Dangnoi Tambom Bantoom	0.088	0.054
9. Ban PhaLuem Tambom Donchang	0.086	0.052
10. Ban PhaChad Tambom Dangyai	0.085	0.051

The results show that Mn-fiber can catch [226]Ra in water supply. The Specific activities of [226]Ra in water supply from Ban Gudnang Tui Tambom Bantoom, Ban Khamhai School Tambon Banped and Banbenggae Tambon Nonton (The red area in Figure 1) are higher than standard values of US Environmental Protection Agency [5, 6] and water supply from Ruenjit Road Tambon Naimeuang, Ban Bengniam Tambon Banbengniam Ban Nhongkha Tambon Nonton and Ban Nongkuay Tambon Thaphra (The orang area in Figure 1) are similar to the standard value. Which should be monitored and find a solution. The Specific activities of [226]Ra in the remaining areas in water supply is lower than standard. The AED values of all regions in Amphoe Muang Khon Kaen is lower than the standard of US Environmental Protection Agency. From results should be a solution in areas with radium higher than standard. Monitoring in areas that radium are close to the standard, because in the long-term, the contamination of [226]Ra in water supply may increase and this can affect the health of people who continuously use the water in the future. Therefore, the behavior of radon in water supply in these areas should be regularly monitored to create security for the people

Conclusions

The [226]Ra concentration in 111 water supply at Amphoe Muang Khon Kaen were determined by measuring activity of [226]Ra via Mn-fiber using gamma spectrometry. The average Specific activities of [226]Ra was found to be 0.038 Bq/l, range 0 – 0.13 Bq/l. The average risk of Annual Equivalent Dose was found to be 0.023 mSv/y, range 0 – 0.079 mSv/y. Some of these results are lower than the standards of US Environmental Protection Agency. But in other areas with [226]Ra higher than standards should be a solution and in areas with [226]Ra close to standard value should be a monitoring. Therefore the water supply in areas with [226]Ra lower than standard of Amphoe Muang Khon Kaen is considered safe to use for consumers. Moreover, this research has shown that Mn-fiber can be used as adsorbent/trap [226]Ra in water for determining [226]Ra contamination in water samples [7].
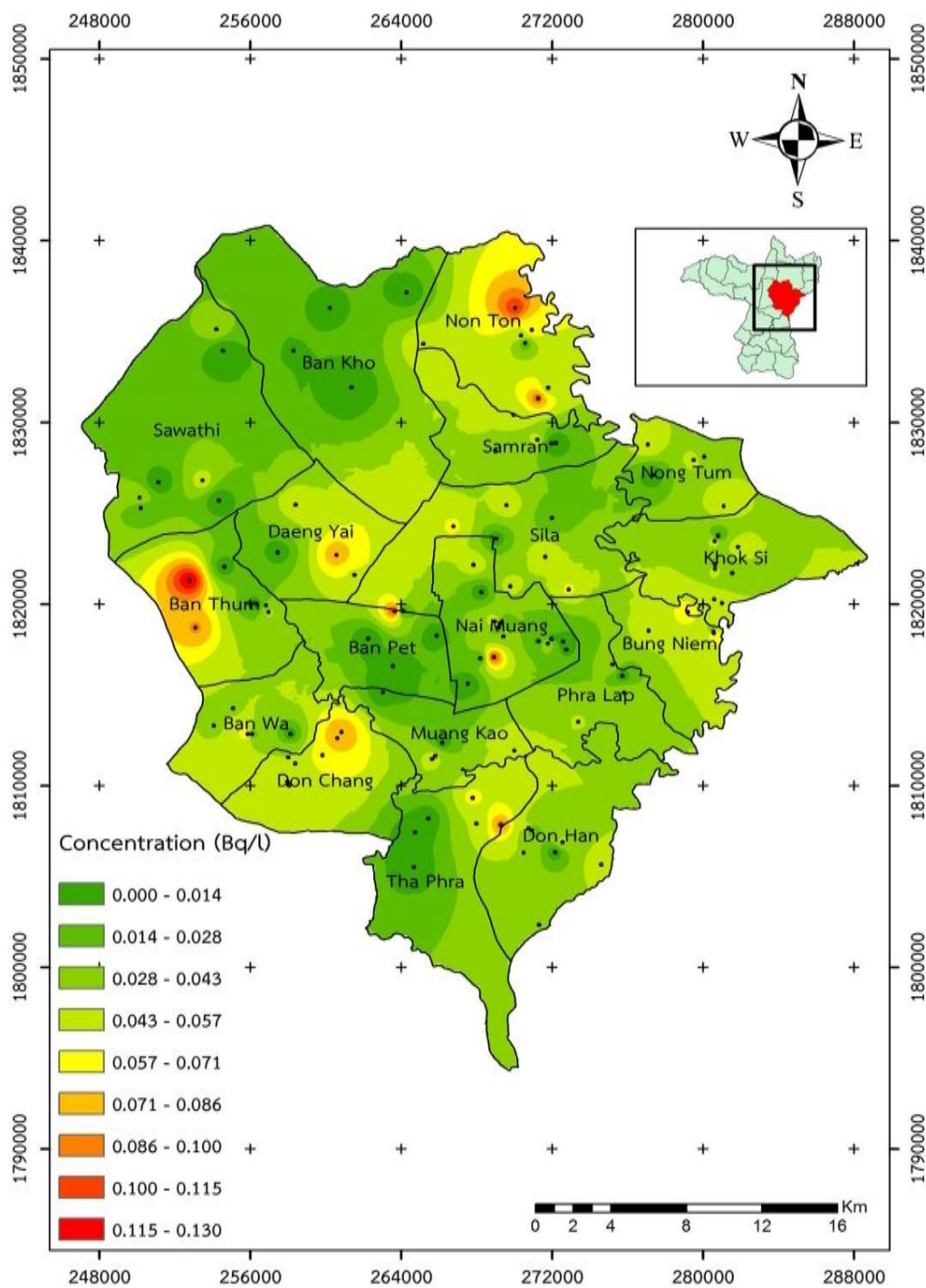
Figure 1 The contour map of ^{226}Ra concentration in water supply at Amphoe Muang KhonKaen

References

[1] Javier Avalos. 2006. **Public Health Goal for Radium-226 and Radium-228 in Drinking Water**. California: USA;. p. 5 - 8.

[2] WHO (World Health Organization). 2011. **Guidelines for Drinking-water Quality**. 4th ed. Geneva: Switzerland.

[3] Egbe Egiebor, Vinay Allagadda. 2014. Evaluation of Uranium and Radium in a Private Well. **Letter Health Consultation**. PITTSYLVANIA, VIRGINIA: USA.

[4] IAEA. 2011. Radiation Protection and Safety of Radiation Sources: **International Basic Safety Standards**, Interim Edition. Vienna (Austria).

[5] Office of Water, U.S. Environmental Protection Agency (USEPA). 2012. **Edition of the Drinking WaterStandards and Health Advisories**. Washington, DC: USA.

[6] B.C. Shivakumara, M.S. Chandrashekara*, E. Kavitha, L. Paramesh. 2014. Studies on ^{226}Ra and ^{222}Rn concentration in drinking water of Mandya region, Karnataka State, India. **Journal of Radiation Research and Applied Sciences 7**: 491 – 498.

[7] Henrieta Dulaiova and William C. Burnett. 2004. An efficient method for γ-spectrometric determination of radium-226, 228 via maganess fibers. **Limnol. Oceanogr: Methods 2**: 256 – 261.

Investigating Rare Events with Modified Monte Carlo Method

Based on Fluctuation Theorem

T. Takol[1*] **and S. Limkumnerd**[1,2**]

[1]Department of Physics, Faculty of Science, Chulalongkorn University, Phayathai Rd., Patumwan, Bangkok 10330, Thailand

[2]Research Center in Thin Film Physics, Thailand Center of Excellence in Physics, CHE, 328 Si Ayutthaya Rd., Bangkok 10400, Thailand

* E-mail: ta_kol.a@hotmail.com

** E-mail: Surachate.l@chula.ac.th

Abstract

The Monte Carlo (MC) method is a useful tool to solve a broad range of problems numerically; random numbers are used to decide whether a process is accepted resulting in a desired equilibrium distribution. In certain complex problems where transitions to some states are rare, however, this method dramatically consumes more resources and spends a long time trying to find the equilibrium states. To improve upon the conventional MC, we apply a fluctuation theorem (FT) to MC which provides a relative weight of a backward trajectory with respect to the forward one. Interestingly, not only does FT double the information but also assist in rapid convergence to an equilibrium distribution. We apply the algorithm to solve a test problem where the energy barrier to a certain state is comparatively high. The result of the simulation is consistent with the analytic solution, but with a significant speed gain compared to that from the conventional method.

Keywords: Monte Carlo method, Fluctuation theorem, Rare events, Rapid convergence

Introduction

Many physics problems cannot be solved analytically. Inevitably, numerical methods which provide approximate the exact solutions, due invoked the iterating nature of these methods, a computational technique is needed. Monte Carlo (MC) method is one of the approximating computational methods that makes use of the probabilistic aspect of a concept of Markov chain. In probability theory, a probability space consists of three parts: a sample space (S) which is a collection all of possible outcomes, a set of events (ω) containing a set of particular outcomes, and probability of an event $(P(\omega))$, which measures how much possibility a particular event is compared to that of other events in the sample space. MC uses a random number to select the next state of a system given the current one. A Markov chain process is defined by the following equation [1].

$$T_{(n|n-1,n-2,..,3,2,1)} = T_{(n|n-1)}, \quad (1)$$

where $T_{(n|n-1)}$ is the conditional probability or the transition probability from state $n-1$ to n. The Markov chain implies that only state $n-1$ is enough to determine the next state of the evolution without any further information from the previous history. With transition probabilities in Markov chain, one can define transition rates at time S, $W_{(i|j)}(s)$, using forward Kolmogorov equation [1, 2],

$$\frac{\partial T_{(i|j)}(s,t)}{\partial t} = \sum_k T_{(i|k)}(s,t)W_{(k|j)}(t),$$

$$\lim_{t \to s} T_{(i|j)}(s,t) = \delta_{ij}, \quad (2)$$

where $T(s,t) = \left[T_{(i|j)}(s,t)\right]$ is a matrix element representing the transition probability to transit from state j to i during time interval t to s; and $W(t) = \left[W_{(i|j)}(t)\right]$ is a transition rate matrix at time t, $W_{(i|j)}(t) = -\sum_{j \neq i} W_{(j|i)}(t)$. It is also equivalent to

$$\lim_{t \to s} \frac{\partial T_{(i|j)}(s,t)}{\partial t} = W_{(i|j)}(t) \quad (3)$$

The evolution of an inhomogeneous Markov process, $x = \{x(t): t_0 \leq t \leq t_N\}$, can be represented by the Master equation [3,4],

$$\frac{\partial P_i(t)}{\partial t} = \sum_j W_{(i|j)}(t)P_j(t) - W_{(j|i)}(t)P_i(t) \qquad (4)$$

Here $P_i(t)$ is the probability distribution of state $i \in S$ at time t. The right-hand side of the equation represents the total probability current. If the total incoming current to state i (first term) is greater than the total outgoing current (second term), the probability at state i increases as time passes. One can view Master equation as an average over changes of states over times or what we call trajectory. A trajectory is therefore defined as a set of states $\{i_1, i_2, \ldots, i_N\} \in S$ that the system jumps to at times $\{t_1, t_2, \ldots, t_N\}$. In an equilibrium state, the left-hand side of the Master equation equals zero. The equilibrium state can then be described by $\sum_j W_{(j|i)}(t)\pi_i = \sum_j W_{(i|j)}(t)\pi_j$, which $\pi_j = \lim_{t \to \infty} P_i(t)$ is the probability distribution of state i at equilibrium [4, 5]. This may be satisfied by imposing detailed balance condition [2, 6, 7]:

$$W_{(j|i)}(t)\pi_i = W_{(i|j)}(t)\pi_j. \qquad (5)$$

The probability fluxes between state i and j are equal. According to Kolmogorov equation, detailed balance from Equation (5) can be written in terms of transition probabilities as follows [2, 8],

$$\lim_{t \to s} T_{(i|j)}(s,t)\pi_i = \lim_{t \to s} T_{(i|j)}(s,t)\pi_i \qquad (6)$$

$$T_{(i|j)}(s,t)\pi_i = T_{(i|j)}(s,t)\pi_i \qquad (7)$$

The most well-known Monte Carlo method named Metropolis Monte Carlo (MC) uses acceptance probability (*Acc*) obeying detailed balance [9, 10]. One uses *Acc* to decide the next step which is either the candidate step or the current state. Approximate equilibrium distributions are obtained by repeating the process. MC process is considerably ineffective if one of the equilibrium probability distribution is rare since the method relies on *Acc* to select the next state, the rare events are hardly accepted. This could be problematic since one may never accrue enough statistics.

In this paper we introduce fluctuation theorem which links the relation between probabilities of forward and backward trajectories. In the latter part of section II, we introduce a new method based on the weight in the previous part in order to cope with the rare-event problems. The comparison between the results from the original MC and that from the new MC along with FT to find probability distribution of rare events at equilibrium are given in section III. Discussion and analysis of the new method compared to traditional MC are discussed in section IV.

Methods

Many physics problems cannot be solved by analytic methods. In order to achieve those results, numerical methods are applied to find the solutions. In this section the approximation algorithm and the new approach are introduced. First, we describe the conventional Metropolis MC algorithm. Then, application of FT to MC is described in the last part of this section.

Metropolis Monte Carlo (MC)

Metropolis Monte Carlo seeks a candidate outcome by a random process, according to an acceptance probability, *Acc*. It is derived from Equation (7) which can be rewritten as,

$$\frac{\pi_i}{\pi_j} = \frac{W_{(i|j)}(t)}{W_{(j|i)}(t)}. \qquad (8)$$

which compares the probability of current state j to the probability of candidate state i by the ratio of transition probabilities between a forward and a backward step. The option of Metropolis MC to define *Acc* for the next step is [9, 11]

$$Acc \equiv \frac{W_{(i|j)}(t)}{W_{(j|i)}(t)} \qquad (9)$$

The procedure of the Metropolis MC algorithm is as follows:

1. Choose an initial configuration.
2. Pick a candidate state randomly.
3. Pick a uniform random number $u \in [0,1]$.
4. Calculate Acc.
5. If $Acc \geq u$, probability distribution is updated by acknowledging the candidate state, else the system stays in the current state.
6. Repeat 2. To 5. until the result reaches the desired accuracy.

Fluctuation Theorem

Fluctuation theorem links the relative probability between the forward and backward trajectories. This is in contrast with MC which only considers only two adjacent

steps in the evolution. The probability of the forward trajectory A is given by [3, 12]

$$P^{\mathrm{F}}[A] = P_{x_0}(t_0)e^{\int_{t_0}^{t_1} dt' W_{(x_0|x_0)}(t')}$$
$$\prod_{t=1}^{N} W_{(x_i|x_{i-1})}(t_i)dt_i e^{\int_{t_i}^{t_{i+1}} dt' W_{(x_i|x_i)}(t')} \quad (10)$$

And a time-reversed trajectory is defined by $x^*(t) = \epsilon x(t_N - t)$, where ϵ is an odd-even operator which gives $+1$ for time-even variable and -1 for time-odd variable. Backward probability, $P^R[A^*]$ can be written as [3,12]

$$P^{\mathrm{R}}[A^*] = P_{x_N}(t_N)e^{\int_{t_0}^{t_1} dt' W_{(\epsilon x_0|\epsilon x_0)}(t')}$$
$$\prod_{t=1}^{N} W_{(\epsilon x_{i-1}|\epsilon x_i)}(t_i)dt_i e^{\int_{t_i}^{t_{i+1}} dt' W_{(\epsilon x_i|\epsilon x_i)}(t')} \quad (11)$$

Due to probabilities of two directions, we can define the entropy change along a trajectory according to [3,7,13-16]

$$\Delta s = \ln(P^{\mathrm{F}}[A]) - \ln(P^{\mathrm{R}}[A^*])$$
$$= \ln\left(\frac{P_{x_0}(t_0)}{P_{x_N}(t_N)}\right) + \sum_{i=0}^{N}\ln\left(\frac{e^{\int_{t_i}^{t_{i+1}} dt' W_{(x_i|x_i)}(t')}}{e^{\int_{t_i}^{t_{i+1}} dt' W_{(\epsilon x_i|\epsilon x_i)}(t')}}\right) +$$
$$\sum_{i=0}^{N}\ln\left(\frac{W_{(x_i|x_{i-1})}(t_i)}{W_{(\epsilon x_{i-1}|\epsilon x_i)}(t_i)}\right) \quad (12)$$

From Equation (3), Equation (12) can be written as follows,

$$\Delta s = \ln\left(\frac{P_{x_0}(t_0)}{P_{x_N}(t_N)}\right) + \sum_{i=0}^{N}\ln\left(\frac{e^{\int_{t_i}^{t_{i+1}} dt' W_{(x_i|x_i)}(t')}}{e^{\int_{t_i}^{t_{i+1}} dt' W_{(\epsilon x_i|\epsilon x_i)}(t')}}\right) +$$
$$\sum_{i=0}^{N}\ln\left(\frac{T_{(x_i|x_{i-1})}(t_i)}{T_{(\epsilon x_{i-1}|\epsilon x_i)}(t_i)}\right) \quad (13)$$

If the probability of a forward trajectory is greater than that of a backward trajectory, the system prefers to evolve into a forward direction and vice versa.

Fluctuation theorem equates the ensemble average of $e^{-\Delta s}$ to one [3]:

$$\langle e^{-\Delta s}\rangle = \sum_A e^{-\Delta s} P^{\mathrm{F}}[A]$$
$$= \sum_A \frac{P^{\mathrm{R}}[A^*]}{P^{\mathrm{F}}[A]} P^{\mathrm{F}}[A] = \sum_A P^{\mathrm{R}}[A^*]$$
$$= 1 \quad (14)$$

We assume that the system obeys detailed balance with constant transition rates, hence, the exponential terms in Equation (13) are canceled. Notice also that,

$$\langle e^{-\Delta s}\delta_{i,x_0}\rangle = \sum_A e^{-\Delta s} P^{\mathrm{F}}[A]\delta_{i,x_0}$$
$$= \sum_A \frac{P_{x_N}(t_N)}{P_{x_0}(t_0)}\prod_{t=1}^{N}\frac{T_{(\epsilon x_{i-1}|\epsilon x_i)}(t_i)}{T_{(x_i|x_{i-1})}(t_i)} P^{\mathrm{F}}[A]\delta_{i,x_0}$$

$$= \sum_A \frac{P_{x_N}(t_N)}{P_{x_0}(t_0)}\prod_{t=1}^{N}\frac{\pi_{x_{i-1}}}{\pi_{x_i}} P^{\mathrm{F}}[A]\delta_{i,x_0}$$
$$= \sum_A \frac{P_{x_N}(t_N)}{P_{x_0}(t_0)}\frac{\pi_{x_0}}{\pi_{x_N}} P^{\mathrm{F}}[A]\delta_{i,x_0}$$
$$= \sum_A \frac{\pi_{x_0}}{P_{x_0}(t_0)} P^{\mathrm{F}}[A]\delta_{ix_0}$$
$$= \sum_{\{x_0=i,x_1,...,x_N\}} \pi_{x_0} e^{\int_{t_0}^{t_1} dt' W_{(x_0|x_0)}(t')}$$
$$\times \prod_{t=1}^{N} W_{(x_i|x_{i-1})}(t_i)dt_i e^{\int_{t_i}^{t_{i+1}} dt' W_{(x_i|x_i)}(t')}$$
$$= \pi_i \quad (15)$$

We can use Equation (15) to find the equilibrium distribution of state i in the simulation.

The Modified MC algorithm

In this part a new MC algorithm is explained. The steady state probability distribution is the destination of a system evolution. Even though, numerical algorithms like metropolis MC can obtain the results, it may take a long time to reach them. Moreover if the transition rate to a particular state is extremely small, the event may never occur during the trial. To achieve the convergent results, we should improve MC by changing the weight of trajectories, using appropriating weight as stated in Equation (15).

This new way of collecting probability of states concerns a trajectory of an evolution. We collect information of a trajectory to calculate $e^{-\Delta s}$ as a weight of a trajectory according to Equation (15). A self-consistent process guides a simulation result to converge to an exact solution of equilibrium distribution. Suppose the transition from i to j is rare, the new method can be used to collect its statistical based on the transition from j to i which is not rare.

1. Choose an initial condition
2. Collect the current state as an initiation of a trajectory.
3. Pick a candidate state randomly.
4. Pick a uniform random number $u \in [0,1]$.
5. Calculate Acc according to Eq.(9).
6. If $Acc \geq u$, collect the candidate state as a part of a trajectory, else collect the current state as a part of a trajectory.
7. Repeat 3. To 6. N times
8. Calculate weight $e^{-\Delta s}$, from an N-step trajectory.

9. The current state or the initiating state of a trajectory, weighed $e^{-\Delta s}$ was updated to probability distribution.

10. Repeat until the result converges to the desired accuracy.

Application and Discussion

Test problem

An evolution of states follows Master equation, Equation (4). In equilibrium $\partial P_i(t)/\partial t = 0$, probabilities of states are fixed because there is no probability current. According to detailed balance which is a stronger condition than equilibrium, every pair of transition in equilibrium obeys,

$$0 = \sum_{j=1}^{n} W_{(i|j)}(t)\pi_j \tag{16}$$

With the Kolmogorov equation and an equilibrium condition, an evolution of a system can be written as $\pi_i = \sum_{j}^{n}(T_{(i|j)}(s,t) - I_{i,j})\pi_j$ or equivalent to

$$0 = \sum_{j}^{n}\big(T_{(i|j)}(s,t) - I_{i,j}\big)\pi_j. \tag{17}$$

Let T be a rare-event matrix [17] where

$$T = \begin{pmatrix} 1-\alpha-\beta & 1/2 & 0 & 1/2 \\ \alpha & 1/2-\gamma & 1/2 & 0 \\ 0 & \gamma & 1/2-\zeta & 1/2 \\ \beta & 0 & \zeta & 0 \end{pmatrix}, \tag{18}$$

$\alpha = e^{-1.5}/2,\ \beta = e^{-20.0}/2,$ and $\zeta = e^{-3.0}/2$.

Its equilibrium distribution is given by

$$p = \begin{pmatrix} 0.81021 \\ 0.18078 \\ 9.0007 \times 10^{-3} \\ 1.6700 \times 10^{-9} \end{pmatrix}. \tag{19}$$

Notice that the fourth state probability is extremely rare.

Simulation Results

In this subsection, we show and discuss results from the traditional MC and the new approach with fluctuation theorem and the rare-event matrix given in, Equation (18). Figure 1 shows the relative errors of four states from the analytical expressions. The filled triangles are the results from the conventional Metropolis MC, while the circles are those of the new algorithm. The simulation generates a trajectory consisting of 1,000,000 states per run. We average the simulation results in each iteration over 3,000 times.
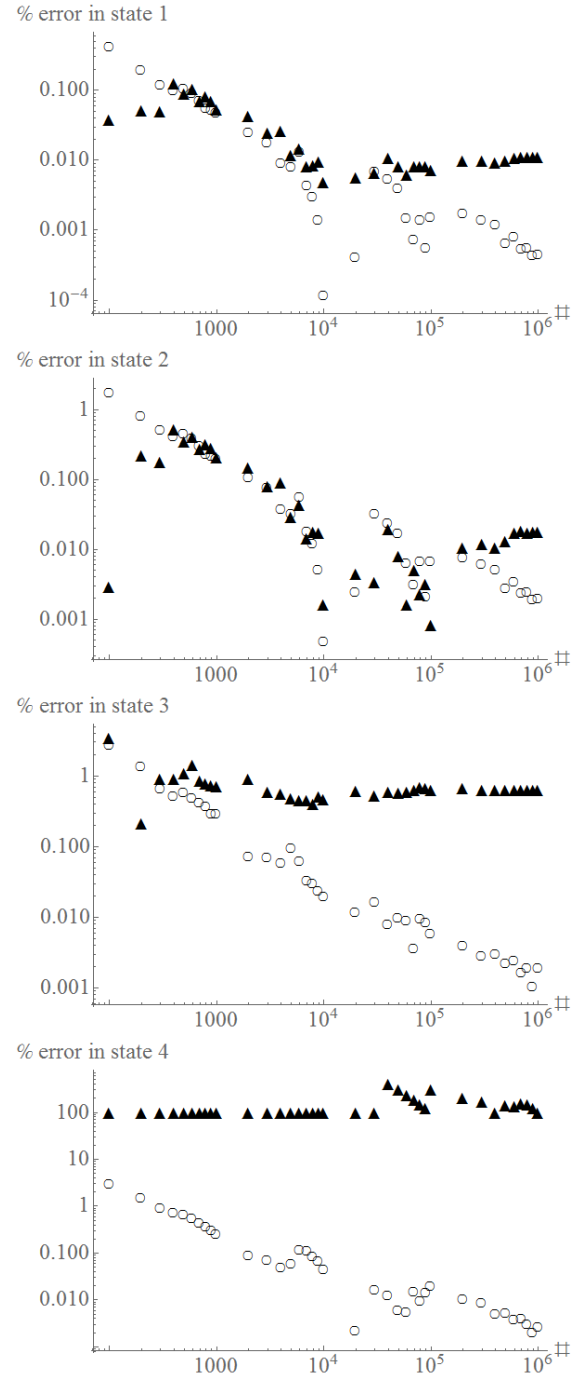

Figure 1 The percent of error in state 1, 2, 3, and 4 from simulation results of MC algorithm (Black triangle dots) and the modified MC algorithm with fluctuation theorem (White circle dots)

According to Metropolis MC algorithm, a randomly selected state is weighed by default value of 1. The accuracy of the results by the algorithm, unavoidably, relies on the number of iterations. With insufficient random samples, this causes two types of mistakes. The rare

states are never found because no count is obtained during the first 10^5 step, hence, the simulation results in 100 % errors. Or MC method accepts a few cases which apparently are too often for the number of trial. This also causes excessive value for the probability distribution in the rare states.

The new approach uses the relative weight from Equation (13) to help resolve the issue. This revolutionizes the traditional MC which concerns only the current state of a system, while the novel method uses information in a relatively abundant trajectory to calculate the weight for rare case. Weighing trajectories by the new algorithm helps reduce the number of iterations and time needed to find the steady state distributions.

Conclusion

The concept of a trajectory leads to the definition of a trajectory probability. With it, we are able to compare the probabilities of occurrence in forward and backward directions. According to the fluctuation theorem, the ratio of forward and its conjugate trajectories also allows us to prove the second law of thermodynamics [16]. We are able to devise a new algorithm to make use of the theorem to compute the equilibrium distributions. The method is especially more superior to the conventional MC in the case where the occurrence of some states is extremely rare.

Acknowledgement

References

[1] W. Feller. "On boundaries and lateral conditions for the Kolmogorov differential equations". **Annals of Mathematics**, 65(3):527-570,1957.

[2] H. Ge, D. Jiang, and M. Qian. "Reversibility and entropy production of inhomogeneous Markov chains". **Journal of Applied Probability**, 43(4):1028-1043, 2006.

[3] M. Esposito and C. Van den Broeck. "Three detailed fluctuation theorems". **Physical Review Letters**, 104:090601, 2010.

[4] M. V. Bonanca and C. Jarzynski. "Conditional reversibility in nonequilibrium stochastic systems". **Physical Review E**, 93(5):022101, 2016.

[5] K. M. Chandy. "The analysis and solutions for general queueing networks". **Proc. Sixth Annual Princeton Conference on Information Sciences and Systems**, Princeton U, 1972.

[6] C. Robert and G. Casella. "Monte Carlo statistical methods". **Springer-Verlag New York**, 2004.

[7] M. Esposito and C. Van den Broeck. "Three faces of the second law. I. Master equation formulation". **Physical Review E**, 82:011143, 2010.

[8] H. Ge, D. Jiang, and M. Qian. "A simple discrete model of Brownian motors: Time periodic Markov chains". **Journal of Statistical Physics**, 123(4):831-859, 2006.

[9] W. K. Hastings. "Monte Carlo sampling methods using Markov chains and their applications". **Biometrika**, 57(1):97-109, 1970.

[10] D. P. Landau and K. Binder. "A Guide to Monte Carlo Simulations in Statistical Physics". **Cambridge University Press**, third edition, 2009. Cambridge Books Online.

[11] F. Wang and D. P. Landau. "Efficient, multiple-range random walk algorithm to calculate the density of states". **Physical Review Letters**, 86:2050-2053, 2001.

[12] R. E. Spinney and I. J. Ford. "Nonequilibrium thermodynamics of stochastic systems with odd and even variables". **Physical Review Letters**, 108:170603, 2012.

[13] J. E. Denis and J. S. Debra. "The fluctuation theorem. Advances in Physics", **Physics Review Letters** 51(7):1529-1585, 2002.

[14] E. M. Sevick, R. Prabhakar, R. W. Stephen, and J. S. Debra. "Fluctuation theorems". **Annual Review of Physical Chemistry**, 59(1):603-633, 2008.

[15] C. Jarzynski. "Hamiltonian derivation of a detailed fluctuation theorem". **Journal of Statistical Physics**, 98(1):77-102, 2000.

[16] J. L. England. "Statistical physics of self-replication". **The Journal of Chemical Physics**, 139(12), 2013.

[17] B. Trendelkamp-Schroer and F. Noe. "Efficient estimation of rare-event kinetics". **Physical Review X**, 6:011009, 2016.

Students' Alternative Conception in Vector Components

with and without Physical Context

U. Wutchana[1,2*]

[1] Department of Curriculum and Instruction, Faculty of Education, Ramkhamkaeng University, Ramkhamhaeng Road,

Bangkapi, Bangkok, 10240, Thailand

[2] Thailand Center of Excellence in Physics, CHE, Ministry of Education, Bangkok, 10240, Thailand

*E-mail: peak_um@hotmail.com, wutchana@ru.ac.th

Abstract

2 open ended problems designed based on research instruments used in physics education research had been used to explore students' conceptual and procedural understanding of vector components. With and without physical context, we asked students to find out magnitude and graphical form of vector components. The problems were given to 211 first year students of faculty of science during the third semester in 2014 academic year. The students spent approximately 15 minutes of their General Physics I course to complete the open ended problems. Consequently, their responses were classified based on the similarity of errors performed in the responses. The study results showed that without physical context, 53.1% of the students provided correct numerical magnitude of vector components while 10.9% of them punctuated the magnitude of vectors in x- with y-component. Others 20.4% provided just symbols and there was no answer of the last 15.6%. When asking to draw graphical form of vector components, only 10.4% of the students made corrections. A majority of them produced errors and revealed alternative conceptions. 46.5% drew longer and/or shorter vector components. 34.6% drew vectors in different form or wrote down other symbols. With physical context, only 6.6% of the students made corrections in numerical magnitude while 6.2% drew longer and/or shorter vector components. Almost all of them (59.7%) drew other force vectors in any axis instead. It indicated that many students did not develop a strong foundation of understanding in vector components and could not apply those concepts to such problems with physical context.

Keywords: Graphical vectors, Vectors, Vector components

Introduction

Previous research had shown that students have difficulties in many concepts of vectors both with and without physical context [1-9]. The research also found that students still hold misconception about vectors although they have studied it before [10-14]. To set up an appropriate teaching approach to enhance their students' understanding, physics instructors need to get some ideas of what alternative conception the students held and what difficulties the students faced. Therefore, we intended to explore students' alternative conception and their ability to apply the vector component concept from mathematics to physics context in this study.

Materials and Methods

The descriptive research has been used. Data collection tool for this study were 2 open ended problems which had been used to explore students' conceptual and procedural understanding of vector components.

Open ended problems

2 equivalent open ended problems with and without physical context had been modified from the work of Deventer and Wittmann [1]. The problems asked students to find out magnitude of component vectors of given vectors $\vec{A}$ and $\vec{N}$, draw graphical vectors of them, and also write down some explanation. The following figure was provided in the problems.
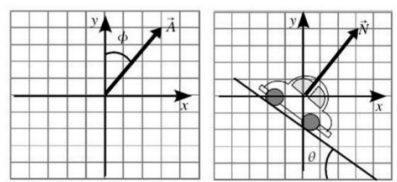
Figure 1 Given vectors with and without physical context for problems 1 and 2 [1]

The Figure 1 shows vector $\vec{A}$ that forms an angle ø with the vertical axis for problem 1 and a car parking on slope area that forms an angle θ with the horizontal axis causing a normal force vector $\vec{N}$ for problem 2.

Data collection

The problems, then, were given to 211 first year students of faculty of science from a large public university in Southern Thailand during the third (summer) semester in 2014 academic year. The students spent approximately 15 minutes of General Physics I course to complete the open ended problem. It was their second time of the course after they had failed in the first semester. Therefore, those students already completed the lesson of vectors before. Consequently, their responses were classified based on the similarity of errors performed in the responses.

Results and Discussion

The students' responses to open ended problems showed that without physical context most students provided correct numerical magnitude of vector components. When asking to draw graphical vectors to represent their answers, a majority of them produce errors and reveal alternative conceptions.

Students' responses to problem 1

53.1% of the students provided correct numerical magnitude of vector components. 10.9% of them punctuated the magnitude of vectors in x-component with y-component. 20.4% of them provided just symbols and there was no answer of the last 15.6%.

Figure 2 shows the students' error responses as punctuation of the vector magnitude and the symbols they wrote.
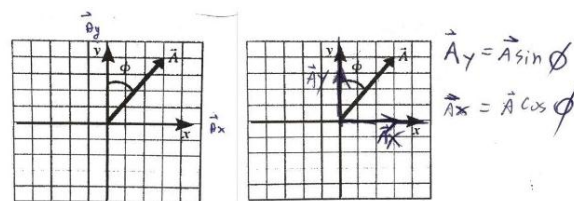

Figure 2 Examples of students' error responses to problem 1

When asking to draw graphical form of vector components, just only 10.4% of the students made corrections. 46.5% of them drew longer and/or shorter vector components. 34.6% drew vectors in different form or wrote down other symbols. 8.5% provided no answer.
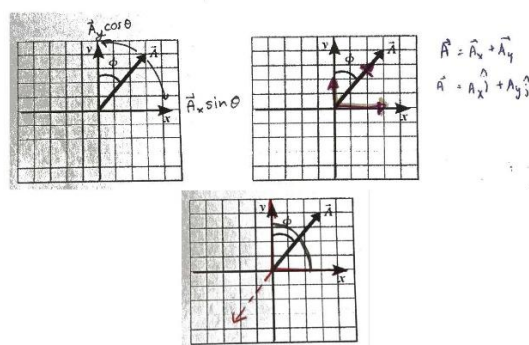

Figure 3 Examples of students' error responses to problem 1

Figure 3 presents the most common errors that students made as drew longer and/or shorter vector, drew vectors in different form, and wrote down other symbols. From this figure, the students seem to be confused the symbols of component magnitude in x- and y-components.

Students' responses to problem 2

With physical context, only 6.6% of the students made corrections in numerical magnitude while the others apply incorrect methods as presented in Figures 4 and 5. Almost all of them drew other force vectors in any axis

instead and try to find out magnitude of vector $\vec{N}$. When asking to draw graphical form of vector components, 59.7% drew other force vectors in any axis instead. 6.2% drew longer and/or shorter vector components. Others 14.2% provided just symbols. The last 19.9% wrote down other symbols or provided no answers to the problem.
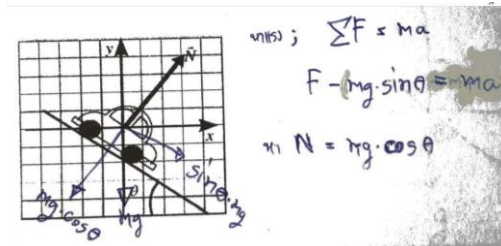

Figure 4 Examples of students' error responses to problem 2

The most common error found in this study is to draw a component with a longer or shorter magnitude. This was also consistent with the work of Zavala and Barniol [3].
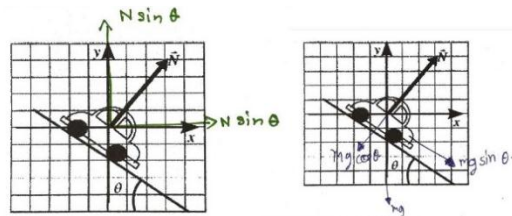
Figure 5 Examples of students' error responses to problem 2

However, in this study also found different results that some students punctuated the magnitude of vectors in x- component with y-component and they confused the symbol of the component magnitude. Most students focused on finding numerical answers even when asking to draw a graphical form of vector component, students try to calculate the numerical magnitude of the normal force vector $\vec{N}$. This may be a consequence of the amount of time instructors spend on algorithms and encouraging students to apply rules to compute its numerical answers, rather than on constructing meaning of the concept.

According to the students' responses, most of the students (67.8%) used different methods on the mathematics and physics context (problems 1 and 2, respectively) as presented in Figure 6. The finding was consistent with the works of Deventer and Wittmann [1] and Barniol and Zavala [4, 9] that students often used different method on equivalent problem in different context.
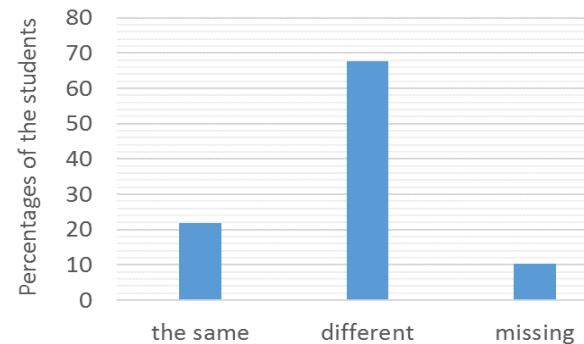

Figure 6 Percentages of students using the same or different methods on problems 1 and 2.

Conclusions

Results from the study showed that students perform worse on a vector component task with and without a physical context. Most students had difficulties with graphical representation. Almost all of them did not develop a strong foundation of understanding in vector component but just learn by memorizing the way to compute its magnitude and attribute little meaning to them. Less of the students could apply vector component concept from mathematics to physics context since they often used different method on different context.

References

[1] Deventer, J. V. & Wittmann, M. C. (2007). Comparing students use of mathematical and physical vector representations. **AIP Conference Proceeding**. 951, 208.

[2] Barniol, P. & Zavala, G. (2009). Investigation of Students' Preconceptions and Difficulties with the Vector Direction Concept at a Mexican University. **AIP Conference Proceedings**, 1179, 85.

[3] Zavala, G. & Barniol, P. (2010). Students' understanding of the concepts of vector components and vector products. **AIP Conference Proceeding**. 1289, 341.

[4] Barniol, P. & Zavala, G. (2010). Vector Addition: Effect of the Context and Position of the Vectors. **AIP Conference Proceedings**, 1289, 73.

[5] Barniol, P. & Zavala, G. (2012). Students' difficulties with unit vectors and scalar multiplication of a vector. **AIP Conference Proceedings**, 1413, 115-118.

[6] Barniol, P., Zavala, G. & Hinojosa, C. (2013). Investigation of Students' Preconceptions and Difficulties with the Vector Direction Concept at a Mexican University. **AIP Conference Proceedings**, 1513, 58-61.

[7] Zavala, G. & Barniol, P. (2013). Students' understanding of dot product as a projection in no-context, work and electric flux problems. **AIP Conference Proceedings**, 1513, 438-441.

[8] Barniol, P. & Zavala, G. (2014). Test of understanding of vectors: a reliable multiple-choice test. **Physical Review Special Topics-Physics Education Research.** 10 (1), 010121.

[9] Barniol, P. & Zavala, G. (2015). Force, velocity, and work: The effects of different contexts on students' understanding of vector concepts using isomorphic problems. **Physical Review Special Topics-Physics Education Research**, 11 (1), 020115-1.

[10] Knight, R. D. (1995). The Vector Knowledge of Beginning Physics Students. **The Physics Teacher**, 33 (2), 74.

[11] Nguyen, N. & Meltzer, D.E. (2003). Initial understanding of vector concepts among students in introductory physics course. **American Journal of Physics**, 71 (6), 630.

[12] Shaffer, P.S. & McDermott, L.C. (2005). A research-based approach to improving student understanding of the vector nature of kinematical concepts. **American Journal of Physics**, 73 (10), 921.

[13] Wutchana, U. & Emarat, N. (2011). Students' Understanding of Graphical Vector Addition in One and Two Dimensions. **Eurasian Journal of Physics and Chemistry**, 3 (2), 102.

[14] Heckler, A.F. & Scaife, T.M. (2015). Adding and subtracting vectors: The problem with the arrow representation. **Physical Review Special Topics-Physics Education Research**, 11 (1), 010101-1.

Dimensional Reduction of Eleven Dimensional Supergravity on SU(2) Group Manifold and N=4 Gauged Supergravity

P. Nuchino[*] and P. Karndumri

Department of Physics, Faculty of Science, Chulalongkorn University, 254 Phayathai Road, Pathumwan, Bankok, 10330

*E-mail: danai.nuchino@hotmail.com

Abstract

The Kaluza-Klein reduction giving rise to four-dimensional N=4, half-maximal SO(4) gauged supergravity from the D=11 supergravity is mainly studied. Apart from some special cases, a Kaluza-Klein sphere reduction is generally not consistent. However, there exists, an alternative way to provide a consistent Kaluza-Klein reduction. The guaranteed-consistent reduction, known as the Scherk-Schwarz reduction, requires doing the dimensional reduction on a group manifold of some particular Lie group. From the fact that the SU(2) group manifold is topologically S^3 embedded in the S^7, the Kaluza-Klein reduction involving S^3 can be obtained from a group manifold reduction via replacing the two S^3 in the reduction ansatz by the two SU(2) group manifolds. The reduction ansatz is guaranteed to be consistent and gives some understanding for the consistency of S^7 reduction. By this reduction ansatz, solutions in four-dimensional N=4 SO(4) gauged supergravity theory can be embedded in 11-dimensional supergravity.

Keywords: Dimensional Reduction, Gauged Supergravity, Kaluza-Klein Reduction, Scherk-Schwarz Reduction

Introduction

Since 1997 that AdS/CFT correspondence, a duality relating supergravities in anti-de Sitter (AdS) background to conformal field theories (CFT) on the AdS boundary [1-3], was first developed, this new duality was becoming a fascinating research topic for many theoretical physicists for a long time. Gauged supergravities, the supergravities with gauged R-symmetry group or any subgroup thereof, admit AdS vacuum solutions that have played the important role in the AdS/CFT correspondence. As mentioned before, a conformal field theory in d spacetime dimensions corresponds with a (d+1)-dimensional gauged supergravity therefore the derivation of gauged supergravity in some specific dimensions becomes valuable for study. In many cases, lower dimensional gauged supergravities can be derived from higher dimensional ungauged supergravities such as the eleven-dimensional supergravity [4], the type IIA and IIB supergravities by using the procedure called dimensional reduction.

Dimensional reduction or Kaluza-Klein reduction [5-8] is the consideration of a gravitational theory in D+n spacetime dimensions where n-dimensional space are compactified to a very small size, in order of Plank length, so the compact space is unobservable at present energy. This unobservable compact space leads to the truncation to the massless sector process giving rise to the lower dimensional gravitational theory with various additional scalar or gauge fields in D dimensions while the symmetry of additional vector fields or gauge fields corresponds to the symmetry on that compact space.

It has been long known that lower-dimensional gauged supergravities can directly be obtained by the Kaluza-Klein reduction on an n-dimensional sphere (S^n) from the higher-dimensional ungauged supergravities as demonstrated in the study of AdS black holes in [9]. Notable cases are the maximal gauged supergravities in 7

and 4 dimensions from Kaluza-Klein reduction on S^4 [10, 11] and S^7 [12] of the eleven-dimensional supergravity and the five-dimensional maximal gauged supergravities from the reduction on S^5 of the type IIB supergravity [13]. The reductions to maximal gauged supergravities are very complicated; the full consistent reduction of S^7 has been recently proven in [14]. On the other hand, many examples giving the half-maximal gauged supergravities in D = 7, 6, 5, and 4 have been worked out completely [15-18].

However, the consistencies of the Kaluza-Klein sphere reductions mentioned above are suspicious. They depend on conspiracies between contributions from the metric and other fields in the higher-dimensional theory and there is no reason for their consistency.

In general, Kaluza-Klein reduction on S^n with arbitrary n>1 leads to be inconsistent. Luckily, there exists an alternative way to perform a reduction. This is known as the Scherk-Schwarz reduction [19] that is guaranteed to be consistent. It is a Kaluza-Klein reduction on a group manifold of a Lie group, a group that satisfies Lie algebra, for example, the group manifold of SU(2) is S^3. On the consistency viewpoint, Lie algebras are classified into 2 types; the Lie algebras with traceless structure constants are referred to as type A where the ansatz is consistent at the level of the higher-dimensional action, while the type B reduction, with non-vanishing trace of structure constants in Lie algebras, is consistent only at the level of the field equations. There are some previous works on this guaranteed consistent reduction. The SU(2) reduction of six-dimensional (1,0) supergravity giving rise to a gauged supergravity in three dimensions was studied in [20], and in a more general case, the group reduction on an n-dimensional group manifold of the ten-dimensional heterotic supergravity is given in [21].

The main purpose of this work is to study the dimensional reduction theory for obtaining the N=4, half-maximal SO(4) gauged supergravity in four-dimensional spacetime by truncating the Kaluza-Klein reduction on S^7 of the ungauged supergravity in 11 dimensions that was

worked out in [18]. However, there are some connections between this non-general consistent reduction and the Scherk-Schwarz reduction that is certainly consistent. In group theory, S^3 is a group manifold of Lie group SU(2). By replacing an S^3 with the SU(2) group manifold and keeping only SU(2) invariant fields, it is guarantee to be a consistent reduction. This could possibly lead us to the more understanding in the consistency of the reduction on S^7.

Besides, knowing the procedure of the dimensional reduction allows us to embed solutions in lower dimensions to higher-dimensional theory through the reduction ansatz as in [22, 23].

Materials and Methods

Dimensional reduction is performed through the reduction ansatze, expressions of the higher dimensional fields in terms of the lower dimensional ones. In supergravity framework, only bosonic parts are sufficiently considered while all fermionic fields can be obtained by supersymmetry transformations. Thus all bosonic fields in both higher and lower dimensional theories are essential materials for the assembly of reduction ansatze.

In this work, the higher dimensional theory is the supergravity in eleven-dimension, a unique maximal-dimensional supergravity. It contains only two bosonic fields:

- the graviton, described by the 11D metric $d\hat{s}_{11}$,
- and a 3-form $\hat{A}_{(3)}$,

where hat fields refer to eleven-dimensional fields.

The bosonic Lagrangian is comprised by the usual Einstein-Hilbert term along with a kinetic term and Chern-Simons term of $\hat{A}_{(3)}$,

$$L_{11} = \hat{R} \,\hat{*} \mathbf{1} - \frac{1}{2} \hat{*} \hat{F}_{(4)} \wedge \hat{F}_{(4)} + \frac{1}{6} \hat{F}_{(4)} \wedge \hat{F}_{(4)} \wedge \hat{A}_{(3)} . \quad (1)$$

Here $\hat{F}_{(4)} = d\hat{A}_{(3)}$ is the field strength 4-form. There are 3 equations of motion in this theory; the first two equations come from the variation of the above Lagrangian (1) with respect to each field,

$$\hat{R}_{MN} = \frac{1}{12}\left(\hat{F}^2_{MN} - \frac{1}{12}\hat{F}^2_{(4)}\hat{g}_{MN}\right), \tag{2}$$

$$d\hat{*}\hat{F}_{(4)} = -\frac{1}{2}\hat{F}_{(4)} \wedge \hat{F}_{(4)}, \tag{3}$$

$$d\hat{F}_{(4)} = 0, \tag{4}$$

where $\hat{R}_{MN}$ is the Ricci tensor describing curvature of the eleven-dimensional spacetime with the coordinate indices $M,N = 0,1,\dots,10$. The last equation (4) is called the Bianchi identity that directly arises from the definition of the field strength 4-form.

While the higher dimensional theory has only two bosonic fields, the four-dimensional N=4 SO(4) gauged supergravity contains more fields;

- the graviton, described by the metric $d\hat{s}_4$,
- the first SU(2) Yang-Mills potentials $A^i_{(1)}$,
- the second SU(2) Yang-Mills potentials $\tilde{A}^i_{(1)}$,
- and two scalar fields;

   the dilaton ϕ and the axion χ,

where i = 1, 2, 3 for each SU(2) Yang-Mills potential.

The bosonic Lagrangian is given by

$$L_4 = R*\mathbf{1} - \frac{1}{2}*d\phi \wedge d\phi - \frac{1}{2}X^4*d\chi \wedge d\chi - V*\mathbf{1}$$
$$- \frac{1}{2}X^{-2}*F^i_{(2)} \wedge F^i_{(2)} - \frac{1}{2}\tilde{X}^{-2}*\tilde{F}^i_{(2)} \wedge \tilde{F}^i_{(2)}$$
$$- \frac{1}{2}\chi F^i_{(2)} \wedge F^i_{(2)} + \frac{1}{2}\chi X^2 \tilde{X}^{-2}\tilde{F}^i_{(2)} \wedge \tilde{F}^i_{(2)}, \tag{5}$$

where

$$X \equiv e^{\frac{1}{2}\phi}, \quad \tilde{X} \equiv X^{-1}q, \quad q^2 \equiv 1 + \chi^2 X^4, \tag{6}$$

the potential V is

$$V = -2g^2\left(4 + X^2 + \tilde{X}^2\right), \tag{7}$$

and the two SU(2) Yang-Mills field strengths are defined by:

$$F^i_{(2)} = dA^i_{(1)} + \frac{1}{2}g\varepsilon_{ijk}A^j_{(1)} \wedge A^k_{(1)}, \tag{8a}$$

$$\tilde{F}^i_{(2)} = d\tilde{A}^i_{(1)} + \frac{1}{2}g\varepsilon_{ijk}\tilde{A}^j_{(1)} \wedge \tilde{A}^k_{(1)}. \tag{8b}$$

The gauge-covariant exterior derivatives, indicating the theory is gauged by each SU(2) gauge group separately, are defined by

$$D\omega^i = d\omega^i + g\varepsilon_{ijk}A^j_{(1)} \wedge \omega^k, \tag{9a}$$

$$\tilde{D}\tilde{\omega}^i = d\tilde{\omega}^i + g\varepsilon_{ijk}\tilde{A}^j_{(1)} \wedge \tilde{\omega}^k, \tag{9b}$$

where the two gauge couplings are chosen to be equal with a constant g, without losing of generality. The two SU(2) together comprise the SO(4) ~ SU(2) × SU(2) gauge group of the N=4 gauged four-dimensional supergravity.

The equations of motion for the scalar field ϕ, which now described by X, and the axion χ are:

$$d\left(X^{-1}*dX\right) = -\frac{1}{2}X^4*d\chi \wedge d\chi + g^2\left(X^2 - X^{-2} + \chi^2 X^2\right)\varepsilon_{(4)}$$
$$+ \frac{1}{4}X^{-2}*F^i_{(2)} \wedge F^i_{(2)} + \frac{1}{2}\chi \tilde{X}^{-4}\tilde{F}^i_{(2)} \wedge \tilde{F}^i_{(2)}$$
$$- \frac{1}{4}\left(1 - \chi^2 X^4\right)X^2 q^{-4}*\tilde{F}^i_{(2)} \wedge \tilde{F}^i_{(2)}, \tag{10}$$

$$d\left(X^4*d\chi\right) = 4g^2\chi X^2 \varepsilon_{(4)} + \frac{1}{2}\left(1 - \chi^2 X^4\right)\tilde{X}^{-4}\tilde{F}^i_{(2)} \wedge \tilde{F}^i_{(2)}$$
$$- \frac{1}{2}F^i_{(2)} \wedge F^i_{(2)} + \chi X^6 q^{-4}*\tilde{F}^i_{(2)} \wedge \tilde{F}^i_{(2)}, \tag{11}$$

where $\varepsilon_{(4)} = \frac{1}{4!}\varepsilon_{\mu\nu\rho\sigma}dx^\mu \wedge dx^\nu \wedge dx^\rho \wedge dx^\sigma$.

The Yang-Mills equations of motion for each SU(2) Yang-Mills field strength are:

$$D\left(X^{-2}*F^i_{(2)}\right) = -d\chi \wedge F^i_{(2)}, \tag{12a}$$

$$\tilde{D}\left(\tilde{X}^{-2}*\tilde{F}^i_{(2)}\right) = d\left(\chi X^2 \tilde{X}^{-2}\right) \wedge \tilde{F}^i_{(2)}, \tag{12b}$$

where D and $\tilde{D}$ are the Yang-Mills-covariant exterior derivatives that were introduced before in (9)

$$DF^i_{(2)} \equiv dF^i_{(2)} + g\varepsilon_{ijk}A^j_{(1)} \wedge F^k_{(2)} = 0, \tag{13a}$$

$$\tilde{D}\tilde{F}^i_{(2)} \equiv d\tilde{F}^i_{(2)} + g\varepsilon_{ijk}\tilde{A}^j_{(1)} \wedge \tilde{F}^k_{(2)} = 0. \tag{13b}$$

These two equations are spontaneously followed from definition of the two SU(2) Yang-Mills field strengths in the same way as the Bianchi identity (4) of the field strength 4-form in eleven-dimensional supergravity.

The last equation of motion is the Einstein equation:

$$R_{\mu\nu} = \frac{1}{2}\partial_\mu\phi\partial_\nu\phi + \frac{1}{2}X^{-2}\left(F^i_{\mu\rho}F^{i\rho}_\nu - \frac{1}{4}\left(F^i_{(2)}\right)^2 g_{\mu\nu}\right) + \frac{1}{2}g_{\mu\nu}V$$
$$+ \frac{1}{2}e^{2\phi}\partial_\mu\chi\partial_\nu\chi + \frac{1}{2}\tilde{X}^{-2}\left(\tilde{F}^i_{\mu\rho}\tilde{F}^{i\rho}_\nu - \frac{1}{4}\left(\tilde{F}^i_{(2)}\right)^2 g_{\mu\nu}\right), \tag{14}$$

where $R_{\mu\nu}$ is called the Ricci tensor in four-dimensional spacetime with the coordinate indices $\mu,\nu = 0,1,\dots,3$.

There are two ways of performing dimensional reduction which respect to the level of consistency of the reduction ansatz.

Firstly, substitutions of reduction ansatze in the Lagrangian of the higher dimensional theory lead to the lower dimensional Lagrangian and in this case the reduction ansatze is said to be consistent at the level of the action.

The second way is the consistency at the level of equations of motion. Reduction ansatze, when substituted into all equations of motion in higher dimensional theory, give rise to the equations of motion in lower dimensional theory.

Results and Discussion

The consistent reduction ansatz for the metric field describes the eleven-dimensional spacetime as a product space between the four-dimensional spacetime and the compact space; seven-dimensional sphere or S^7 where its geometry can be described as a foliation of S^3 x S^3. By the fact that S^3 is the group manifold of the Lie group SU(2), the parts of reduction ansatz involving S^3 can be obtained from the Scherk-Schwarz reduction. Therefore the whole reduction ansatz are

$$d\hat{s}_{11}^2 = \Delta^{2/3} ds_4^2 + 2g^{-2}\Delta^{2/3} d\xi^2$$
$$+ \frac{1}{2}g^{-2}\Delta^{2/3}\left[\frac{c^2}{c^2 X^2 + s^2}\sum_i (h^i)^2 + \frac{s^2}{s^2 \tilde{X}^2 + c^2}\sum_i (\tilde{h}^i)^2\right],$$

(15)

where

$$\Delta \equiv \left[(c^2 X^2 + s^2)(s^2 \tilde{X}^2 + c^2)\right]^{\frac{1}{2}}, \qquad (16)$$

$$c \equiv cos\xi, \quad s \equiv sin\xi, \qquad (17)$$

$$h^i \equiv \sigma_i - gA_{(1)}^i, \quad \tilde{h}^i \equiv \tilde{\sigma}_i - g\tilde{A}_{(1)}^i. \qquad (18)$$

The three quantities, σ_i and $\tilde{\sigma}_i$, are left-invariant 1-forms on each S^3 that satisfy the relations:

$$d\sigma_i = -\frac{1}{2}\varepsilon_{ijk}\sigma_j \wedge \sigma_k, \quad d\tilde{\sigma}_i = -\frac{1}{2}\varepsilon_{ijk}\tilde{\sigma}_j \wedge \tilde{\sigma}_k. \qquad (19)$$

It is more explicit to consider geometry of the spacetime in the "unexcited" state that the both SU(2) gauge fields, axion, and dilaton vanish

$$X = \tilde{X} = 1, \qquad (20)$$

$$\Delta \equiv \left[(c^2 + s^2)(s^2 + c^2)\right]^{\frac{1}{2}} = 1, \qquad (21)$$

$$h^i \equiv \sigma_i, \quad \tilde{h}^i \equiv \tilde{\sigma}_i. \qquad (22)$$

The metric reduction ansatz will becomes

$$d\hat{s}_{11}^2 = ds_4^2 + 2g^{-2}\left[d\xi^2 + cos^2\xi \frac{1}{4}\sum_i (\sigma^i)^2 + sin^2\xi \frac{1}{4}\sum_i (\tilde{\sigma}^i)^2\right],$$

(23)

where $\frac{1}{4}\sum_i (\sigma^i)^2$ and $\frac{1}{4}\sum_i (\tilde{\sigma}^i)^2$ are metrics on the two unit S^3 and the terms in the bracket are the metric on the unit S^7 (the internal space);

$$d\Omega_7^2 = d\xi^2 + cos^2\xi \frac{1}{4}\sum_i (\sigma^i)^2 + sin^2\xi \frac{1}{4}\sum_i (\tilde{\sigma}^i)^2, \qquad (24)$$

while the "latitude" coordinate ξ running between the limits $0 \le \xi \le \frac{\pi}{2}$, at which one of the two S^3 shrinks to zero radius. Remarkably, all four-dimensional equations of motions obtained from the reduction ansatze need to be independent on this latitude coordinate to achieve the consistency.

In this state, the metric ansatz in (23) is clearly describing the compact space as a round S^7 with radius $\sqrt{2}/g$. On the other hand, the existence of other fields distorts the shape of the round S^7.

While the consistent reduction ansatz of the eleven-dimensional metric is derived by using the assistance from the SU(2) group reduction, the 4-form field strength ansatz are determined by a trial and error process introducing additional terms from the already known reduction ansatz in the abelian case until the dimensional reduction are finally consistent. The reduction ansatz for the 4-form field strength is given by:

$$\tilde{F}_{(4)} = -g\sqrt{2}\left(X^2c^2 + \tilde{X}^2s^2 + 2\right)\varepsilon_{(4)} - \frac{4sc}{g\sqrt{2}} X^{-1} * dX \wedge d\xi$$

$$+ \frac{\sqrt{2}\,sc}{g} \chi X^4 * d\chi \wedge d\xi + \frac{\partial f}{\partial \chi} d\chi \wedge \varepsilon_{(3)}$$

$$+ \frac{\partial f}{\partial X} dX \wedge \varepsilon_{(3)} + \frac{\partial f}{\partial \xi} d\xi \wedge \varepsilon_{(3)} + \frac{\partial \tilde{f}}{\partial \chi} d\chi \wedge \tilde{\varepsilon}_{(3)}$$

$$+ \frac{\partial \tilde{f}}{\partial X} dX \wedge \tilde{\varepsilon}_{(3)} + \frac{\partial \tilde{f}}{\partial \xi} d\xi \wedge \tilde{\varepsilon}_{(3)}$$

$$- \frac{1}{2} f g\, \varepsilon_{ijk} h^i \wedge h^j \wedge F_{(2)}^k - \frac{1}{2} \tilde{f} g\, \varepsilon_{ijk} \tilde{h}^i \wedge \tilde{h}^j \wedge \tilde{F}_{(2)}^k$$

$$+ \frac{1}{\sqrt{2}g^2}
\begin{bmatrix}
sc\, X^{-2} d\xi \wedge h^i \wedge *F_{(2)}^i \\
+ \frac{1}{4} c^2 X^{-2} \varepsilon_{ijk} h^i \wedge h^j \wedge *F_{(2)}^k \\
- sc\, \tilde{X}^{-2} d\xi \wedge \tilde{h}^i \wedge *\tilde{F}_{(2)}^i \\
+ \frac{1}{4} s^2 \tilde{X}^{-2} \varepsilon_{ijk} \tilde{h}^i \wedge \tilde{h}^j \wedge *\tilde{F}_{(2)}^k \\
+ sc\, \chi\, d\xi \wedge h^i \wedge F_{(2)}^i \\
+ \frac{1}{4} c^2 \chi\, \varepsilon_{ijk} h^i \wedge h^j \wedge F_{(2)}^k \\
+ sc\, X^2 \tilde{X}^{-2} d\xi \wedge \tilde{h}^i \wedge \tilde{F}_{(2)}^i \\
- \frac{1}{4} s^2 \chi\, X^2 \tilde{X}^{-2} \varepsilon_{ijk} \tilde{h}^i \wedge \tilde{h}^j \wedge \tilde{F}_{(2)}^k
\end{bmatrix} \qquad (25)$$

where

$$\varepsilon_{(3)} = \frac{1}{6} \varepsilon_{ijk} h^i \wedge h^j \wedge h^k \,, \qquad (26a)$$

$$\tilde{\varepsilon}_{(3)} = \frac{1}{6} \varepsilon_{ijk} \tilde{h}^i \wedge \tilde{h}^j \wedge \tilde{h}^k \,, \qquad (26b)$$

$$f = \frac{1}{2\sqrt{2}} g^{-3} c^4 \chi\, X^2 \left(c^2 X^2 + s^2\right)^{-1} \,, \qquad (27a)$$

$$\tilde{f} = -\frac{1}{2\sqrt{2}} g^{-3} s^4 \chi\, X^2 \left(s^2 \tilde{X}^2 + c^2\right)^{-1} \,. \qquad (27b)$$

These metric reduction ansatz (15) and (25) are invariant under a residual Z_2 subgroup of the original global SL(2,R) symmetry of the ungauged four-dimensional N=4 supergravity that transforms the various quantities to their primed image by

$$X' = \tilde{X}, \quad \left(\chi X^2\right)' = -\chi X^2, \qquad (28)$$

$$A_{(1)}^{\prime i} = \tilde{A}_{(1)}^i, \quad \tilde{A}_{(1)}^{\prime i} = A_{(1)}^i, \qquad (29)$$

$$c' = s, \quad s' = -c, \qquad (30)$$

$$\Delta' = \Delta, \quad q' = q, \qquad (31)$$

$$h_i' = \tilde{h}_i, \quad \tilde{h}_i' = h_i, \qquad (32)$$

$$\varepsilon_{(3)}' = \tilde{\varepsilon}_{(3)}, \quad \tilde{\varepsilon}_{(3)}' = \varepsilon_{(3)}. \qquad (33)$$

This residual Z_2 corresponds to an interchange of the two S^3 in the foliation of $S^3 \times S^3$ describing the compact space S^7. In the four-dimensional theory, it involves an interchange of the two SU(2) gauge fields.

Substitutions of the reduction ansatze (15) and (25) into the three equations of motion for the eleven-dimensional supergravity (2)-(4) yield all four-dimensional

equations of motion for N=4, SO(4) gauged supergravity (10)-(14), which imply this dimensional reduction is consistent only at the level of equations of motion.

The obvious reason why this dimensional reduction only works at the level of equations of motion is the ansatz for anti-symmetric tensor is made on the 4-form field strength (25), rather than on the 3-form potential $\hat{A}_{(3)}$, such that the explicit form of $\hat{A}_{(3)}$ cannot directly be derived from this ansatz. As a result, the last Chern-Simons term in the bosonic Lagrangian of the eleven-dimensional supergravity (1) cannot be reduced by these reduction ansatz.

However, the consistency at the level of equations of motion from this reduction is enough for studying embedding of the four-dimensional solutions in eleven dimensions. Since all solutions must satisfy equations of motion in each theory, solutions in one theory are also the solutions in another one through these reduction ansatz.

Conclusions

The consistent dimensional reduction giving rise to four-dimensional N=4 SO(4) gauged supergravity from the supergravity in eleven dimensions is achieved. The reduction ansatz for the metric field are gorgeously described by symmetry of the SO(4) ~ SU(2) x SU(2) gauge group when each term involving SU(2) is obtained by the Scherk-Schwartz reduction that is guaranteed to be consistent. However, this consistency is still suspicious. It relies on the conspiracy between the contributions from the 4-form and the metric reduction ansatze to obtain the consistency reduction without another reason.

Nevertheless, the consistency at the level of the equations of motion of the dimensional reduction allows us to embed or oxidize any solutions of the four-dimensional N=4 SO(4) gauged supergravity in the more fundamental theory, the supergravity in 11 dimensions. It is more convenient to study some solutions in eleven-dimensional theory that has less field content than the lower-dimensional one.

References

[1] Maldacena, J. 1998. "The large N limit of superconformal field theories and supergravity". **Advances in Theoretical and Mathematical Physics**. 2: 231-252.

[2] Gubser, S. S., Klebanov, I. R., and Polyakov, A. M. 1998. "Gauge theory correlators from noncritical string theory". **Physics Letters B**. 428: 105-114.

[3] Witten, E. 1998. "Anti-de Sitter space and holography". **Advances in Theoretical and Mathematical Physics**. 2: 253-291.

[4] Cremmer, E., Julia, B., and Scherk, J. 1978. "Supergravity Theory in Eleven-Dimensions". **Physics Letters B**. 76: 409-412.

[5] Nordstrom, G. 1914. "On the possibility of a unification of the electromagnetic and gravitational fields". **Physik Zeitschr**. 15: 504-506.

[6] Kaluza, T. 1921. "On the unity problem in physics". **Sitzungsberichte der K. Preussischen Akademie der Wissenschaften zu Berlin**. 966-972.

[7] Appelquist, T., Chodos, A., and Freund, P. G.O. 1987. **Modern Kaluza-Klein Theories**. California: Addison-Wesley.

[8] Pope, C. N. "Kaluza-Klein Theory". **http://people.physics.tamu.edu/pope/ihplec.pdf**. [Online; accessed 6-January-2016].

[9] Cvetic, M., *et al*. 1999. "Embedding AdS Black Holes in Ten and Eleven Dimensions". **Nuclear Physics B**. 558: 96-126.

[10] Nastase, H., Vaman, D., and Nieuwenhuizen, P. V. 1999. "Consistent nonlinear KK reduction of 11d supergravity on $AdS_7{\times}S^4$ and self-duality in odd dimensions". **Physics Letters B**. 469: 96-102.

[11] Nastase, H., Vaman, D., and Nieuwenhuizen, P. V. 2000. "Consistent of the $AdS_7{\times}S^4$ reduction and the origin of self-duality in odd dimensions". **Nuclear Physics B**. 581: 179-239.

[12] De Witt, B. and Nicolai, H. 1987. "The consistency of the S^7 truncation in D=11 supergravity". **Nuclear Physics B**. 281: 211-240.

[13] Baguet, A., Hohm, O., and Samtleben, H. 2015. "Consistency type IIB reductions to maximal 5D supergravity". **Physical Review D**. 92: 065004.

[14] Varela, O. 2015. "The complete D=11 embedding of SO(8) supergravity". **arXiv:1512.04943**. [Online; accessed 5-may-2016].

[15] Lu, H., Pope, and C. N. 1999. "Exact Embedding of N=1, D=7 Gauged Supergravity in D=11". **Physics Letters B**. 467: 67-72.

[16] Cvetic, M., Lu, H. and Pope, C. N. 1999. "Gauged Six-dimensional Supergravity from Massive Type IIA". **Physical Review Letters**. 83: 5226-5229.

[17] Lu, H., Pope, C. N., and Tran, T. A. 2000. "Five-dimensional N=4, SU(2) × U(1) Gauged Supergravity from type IIB". **Physics Letters B**. 475: 261-268.

[18] Cvetic, M., Lu, H. and Pope, C. N. 2000. "Four-dimensional N=4 SO(4) Gauged Supergravity from D=11". **Nuclear Physics B**. 574: 761-781.

[19] Scherk, J. and Schwarz, J. H. 1979. "How to get masses from extra dimensions". **Nuclear Physics B**. 153: 61-88.

[20] Lu, H., Pope, C. N., and Sezgin, E. 2003. "SU(2) Reduction of Six-dimensional (1,0) Supergravity". **Nuclear Physics B**. 668: 237-257.

[21] Lu, H., Pope, C. N., and Sezgin, E. 2007. "Group Reduction of Heterotic Supergravity". **Nuclear Physics B**. 772: 205-226.

[22] Hernandez, H. H., and Morales-Tecoti, H. A. 2003. "New Solution of D=11 Supergravity on S^7 from D=4". **Journal of High Energy Physics**. 2003: 039

[23] Lu, H., and Zhang, X. 2014. "Exact Collapse Solutions in D=4, N=4 Gauged Supergravity and Their Generalizations". **Journal of High Energy Physics**. 2014: 099

Spectroscopic Studies of Ruby and Pink Sapphire Samples

P. Chompu and W. Wongkokua*

Department of Physics, Faculty of Science, Kasetsart University, 50 Ngam Wong Wan Rd., Chatuchak,

Bangkok, 10900 Thailand

*E-mail: wiwat.w@ku.ac.th

Abstract

X-ray fluorescent spectrometry and UV-vis spectroscopy are advanced techniques that can be used to characterize gem materials. Transition metal defects are causes of colors in corundum. Fe and Ti are the causes of the blue color in blue sapphire while Cr is the cause of the colors in ruby and pink sapphire. In this work, we investigated the differentiation between ruby and pink sapphire samples. The amount of Cr, Ti, Fe and V were analyzed by x-ray fluorescent spectrometry. The concentrations of the defects were calibrated using NIST 610 standard reference material (SRM) and laser ablation inductively coupled plasma mass spectrometry (LA-ICP-MS). The optical characteristics were analyzed by the UV-vis spectroscopic technique.

Keywords: Corundum, Ruby, Pink Sapphire, X-ray fluorescent spectrometry, UV-vis spectroscopy

Introduction

Corundum or aluminium oxide, Al_2O_3, is a gem material known as ruby and sapphires. The crystal structure is trigonal that is a subsystem of the hexagonal system. The pristine corundum is colorless. The causes of the colors in corundum are transition metal elements that substitute aluminiums in the crystal structure [1].

Most colors of sapphires are caused by Fe and Ti impurities such as blue sapphire caused by Fe and Ti pairs of ions [2, 3] and yellow sapphire is caused by Fe ions [1]. The green color of green sapphire is caused by the mixture between the blue and yellow sapphires [4]. The red color of ruby is caused by Cr [5]. The purple color is caused by the mixture between the red color of ruby and the blue color of blue sapphire [6]. However, the color of pink sapphire can be caused by both Cr [7] and Ti [8].

In this paper, we investigated the differentiation of the causes of the colors between ruby and pink sapphires. The amount of transition metal elements were investigated by x-ray florescent spectrometry. The causes of the colors of ruby and pink sapphire samples were characterized by UV-vis spectroscopy.

Materials and Methods

We used fifteen faceted sapphire samples including thirteen natural and two synthetic sapphires. The samples were arranged and labeled by the colors form low to high intensities by naked eye. All of the samples were collected from gem stone markets in Bangkok, Thailand.

The UV-Vis absorption measurements were carried out using a PerkinElmer UV-Vis spectrometer Lambda^{TM} 650 with a 60 mm integrating sphere with the range of 300 nm to 800 nm. The absorption spectra

were collected in transmission mode at room temperature.

    We measured the contents of Cr, Ti, Fe and V using an energy dispersive x-ray fluorescence spectrometer (EDXRF) EAGLE III[TM]. The contents were calibrated against NIST610 standard reference material (SRM) and laser ablation inductively couple plasma mass spectrometry (LA-ICP-MS).
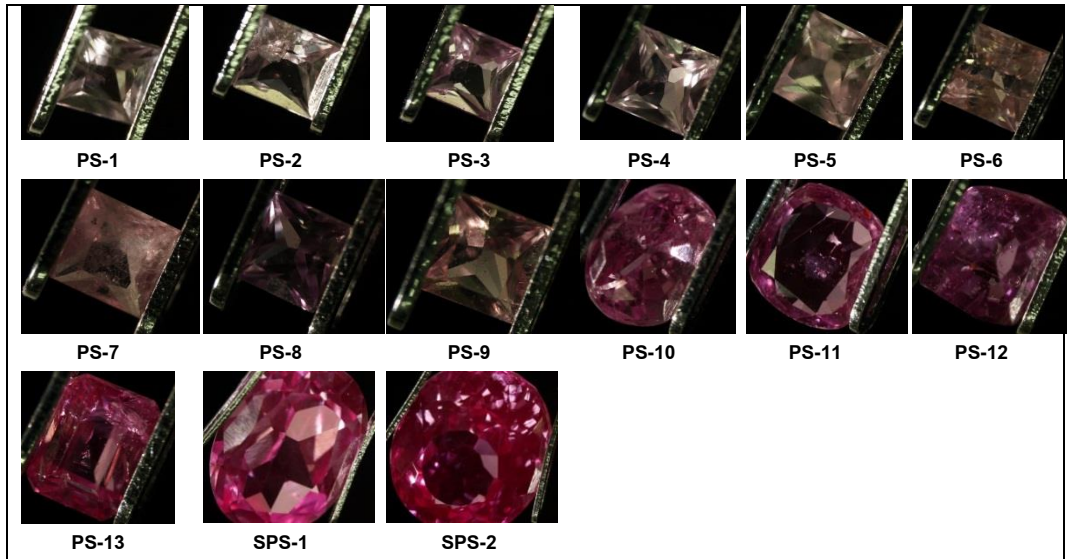

Figure 1 Varieties of sapphire samples chosen for the experiment. The samples were labeled PS for natural sapphires and SPS for synthetic sapphires.

Results and Discussion

    The x-ray fluorescent exited energy of Rh was 40 keV. The selected XRF spectra of the sapphire samples with the peaks of Ti, Cr, Fe and V are shown in Figure 2. The contents of the elements can be calculated using the area under the curves evaluated by PyMca software [3, 9]. The XRF spectra were normalized by the areas of Al and multiplied by calibration factors providing the transition metal element concentration as shown in Table 1. Relative standard uncertainties of concentration were 14%, 45%, 37% and 23% for Ti, Cr, Fe and V respectively. The concentration of Ti was higher than Cr in PS-1 to PS-8 natural samples and SPS-1 synthetic sample. The concentration of Cr was higher than Ti in PS-9 to PS-13 natural samples and SPS-2 synthetic sample. The concentration of Fe and V were not correlated to the causes of the pink color of the pink sapphires and the red color of the ruby samples. The concentration of the transition metal element is given by

$$C_i = \left[\frac{A_{nr}}{A_r} \times LAICPMS \right] \frac{A_i}{A_n} \qquad (1)$$

where

    A_r is the fitted area of transition metal elements of the referent sample

    A_{nr} is the normalized fitted area of the referent sample

    LAICPMS is the contents of the elements obtained from the SRM and LA-ICP-MS

    A_i is the fitted area of the ith transition metal element of the sample

    A_n is the normalized fitted area of the sample
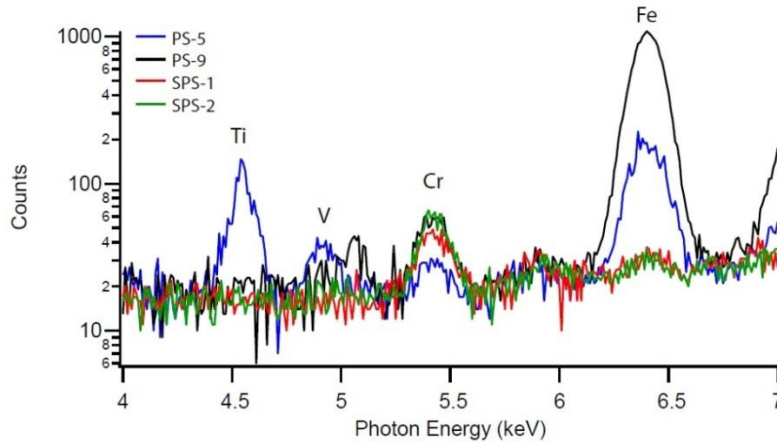
Figure 2 XRF spectra of sapphire samples using 40.0 keV x-ray excited energy.

Table 1 The amounts of Cr, Ti, Fe and V in samples, as determined by x-ray fluorescence.

Samples	Concentration (mg kg^{-1})			
	Cr	Ti	Fe	V
PS-1	38.5	270.4	560.2	14.7
PS-2	54.6	268.2	868.1	2.4
PS-3	95.6	1383.8	814.4	28.0
PS-4	48.4	233.3	553.4	2.2
PS-5	63.1	3092.7	1020.4	137.4
PS-6	60.5	320.8	912.3	30.1
PS-7	178.3	973.3	2648.3	86.2
PS-8	222.0	652.1	2752.8	29.5
PS-9	208.1	86.9	5755.6	96.4
PS-10	151.7	71.2	407.0	2.5
PS-11	157.7	28.1	400.7	0.6
PS-12	188.6	76.8	353.1	6.3
PS-13	383.7	14.4	126.0	112.7
SPS-1	77.1	107.5	14.0	3.7
SPS-2	101.3	35.3	15.3	3.8

UV-vis spectra of two natural sapphires PS-5, PS-9 and two synthetic sapphires SPS-1, SPS-2 are shown in Figure 3. The spectra show absorption bands of Cr^{3+} at 405 nm and 556 nm and a fluorescent peak at 694 nm [10, 11], which are violet-blue, green-yellow and orange colors, respectively. The combination between the absorption bands and the fluorescent peak of Cr^{3+} yield the pink-red color. Absorption peaks at 377 nm,

388 nm, 450 nm of PS-5 and PS-9 are caused by Fe^{3+} [3, 10].

We found that the pink-red colors of the samples trended to increase the intensities when the concentration of Cr^{3+} increased in both natural and synthetic samples. We found no correlation between the concentration of Ti and the colors of the samples. In the synthetic samples, the concentrations of Cr^{3+}

were lower than the natural samples but the color intensities were higher. Hence, the intensities of the color dominated by the arrangement of the Cr^{3+} rather than the concentrations.

There was no absorption band of Ti in the UV-vis spectra of the samples. The Ti can cause the pale pink color in synthetic sapphire [2]. The oxidation state of Ti was suggested to be Ti^{3+} for the pink sapphires grown by Czochralski-pulled process [8]. Hence, the oxidation state of Ti of the samples was Ti^{4+} and synthesized by Flame-Fusion method for the synthetic samples [12].

The Fe^{3+} and Ti^{4+} pairs are the cause of the blue color in blue sapphire [3]. The concentrations of Fe^{3+} and Ti^{4+} in the samples were sufficient to cause the blue color. However, the colors of the samples were not blue because the Fe^{3+} and Ti^{4+} were separated.

The concentration of Cr that less than 1000 mg kg^{-1} was classified as pink sapphire [7]. However, form our results the arrangement of Cr as single Cr^{3+} in the samples was dominated for the pink-red colors as seen in synthetic samples. Hence, we suggest that the UV-vis spectroscopic method such as CIELAB color indices is a better choice to classify between pink sapphire and ruby.
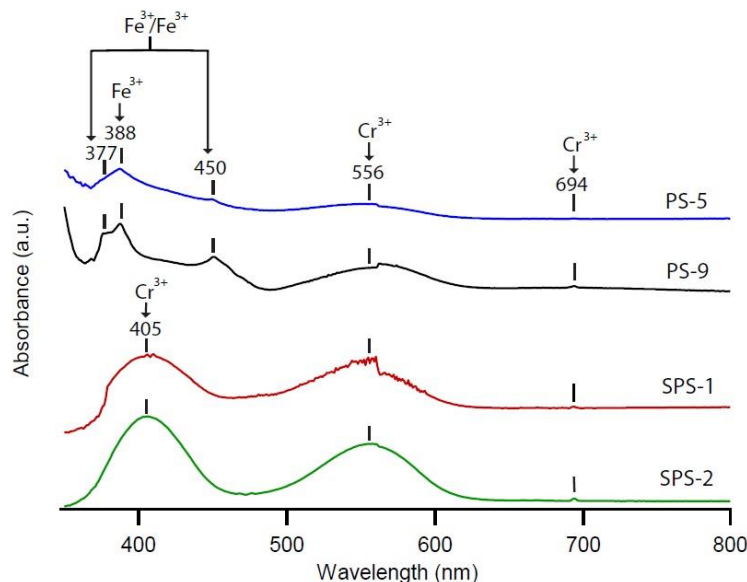
Figure 3 UV-vis absorption spectra of corundum samples show peaks of Cr^{3+}, Fe^{3+}, Fe^{3+}/Fe^{3+}.

Conclusions

Fifteen sapphire samples with different origin including natural and synthetic sapphires collected to study the cause of the colors for differentiation between the pink sapphires and the ruby samples. Cr was the cause of the pink-red color. The concentration of Cr could not classify the pink sapphire and ruby samples. We suggest the UV-vis spectroscopic method to differentiate between pink sapphires and ruby.

Acknowledgments

References

[1] Nassau, K. 1983. **The Physics and Chemistry of Color: The Fifteen Causes of Color.** John Wiley & Sons, Inc., New York.

[2] Townsend, M.G. 1968. Visible charge transfer band in blue sapphire. **Solid State Communications.** 6: 81-83.

[3] Wongrawang, P., N Monarumit, N Thammajak, P Wathanakul and W Wongkokua. 2016. Oxidation states of Fe and Ti in blue sapphire. **Materials Research Express.** 3, 026201.

[4] Winotai, P., S. Saiseng and T. Sudyoadsuk. 2001. Optimization of heat treatments of African green sapphires. **Modern Physics Letters B.** 15: 873-882.

[5] Muhlmeister, Sam., Emmanuel Fritsch, James E. Shigley, Bertrand Devouard and Brendan M. Laurs. 1998. Separating natural and synthetic rubies on the basic of trace-element chemistry. **Gems & Gemology.** 34: 80-101.

[6] Mungchamnankit, A., T. Kittiauchawal, J. Kaewkhao and P. Limsuwan. 2012. The Color Change of Natural Green Sapphires by Heat Treatment. **Procedia Engineering.** 32: 950-955.

[7] Sorokina, Elena S., Andrey K. Litvinenko, Wolfgang Hofmeister, Tobias Häger, Dorrit E. Jacob, and Zamoniddin Z. Nasriddinov. 2015. Rubies and Sapphires from Snezhnoe, Tajikistan. **Gems & Gemology.** 51: 160-175.

[8] Johnson, Mary L., Meredith E. Mercer, Emmanuel Fritsch, Patricia Maddison and James E. Shigley. 1995. "Ti-Sapphire": Czochralski-pulled synthetic pink sapphire from union carbide. **Gems & Gemology**. 31: 188-195.

[9] Solé, V.A., E. Papillon, M. Cotte, Ph. Walter and J. Susini. 2007. A multiplatform code for the analysis of energy-dispersive X-ray fluorescence spectra. **Spectrochimica Acta Part B**. 62: 63-68.

[10] Emmett, John L., Kenneth Scarratt, Shane F. McClure, Thomas Moses, Troy R. Douthit, Richard Hughes, Steven Novak, James E. Shigley, Wuyi Wang, Owen Bordelon and Robert E. Kane. 2003. Beryllium diffusion of ruby and sapphire. **Gems & Gemology.** 39: 84-135.

[11] Wongkokua, W., S Pongkrapan, P Dararutana, J T-Thienprasert and P Wathanakul. 2009. X-ray absorption near-edge structure of chromium ions in α-Al_2O_3. **J. Phys.: Conf. Ser.** 185, 012054.

[12] Kawaminami, Shuichi., Keisuke Mochizuki, Shinobu Hashimoto, Nobuyasu Adachi and Toshitaka Ota. 2013. Coloration of Ti-doped sapphire grown by the Flame-Fusion Method. **Journal of Asian Ceramic Societies.** 1: 362-367.

The Effects of Cathodic Arc Parameter on Color and Hardness of ZrN Thin Films Decorative Coating

Y. Pholrong[1*], P. Chityuttakan[1], C. Luangchaisri[1] and J. Liammukda[2]

[1]Department of Physics, Faculty of Science, King Mongkut's University of Technology Thonburi,

126 Pracha Uthit Rd., Thung Khru, Bangkok, 10140, Thailand

[2]Salamander Jewelry Co., Ltd. 128/1 Moo.7, Soi Wat Nakhon Chuenchum, Phutthamonthon Sai 4 Rd. Tambon Kratumlom,

Ampur Sampran, Nakhon Pathom 73220

*E-mail: naiyots60@gmail.com

Abstract

This research presents the effects of deposition parameter on zirconium nitride (ZrN) thin film coated on stainless steel by cathodic arc technique. For the jewelry applications, the ZrN films must have the high hardness with high gold color. The deposition parameter in this work consists of input voltage supplied to substrate, percent of duty cycle, flow rate of nitrogen gas and deposition time. The as grown ZrN thin films characterized using several techniques. The structural properties were analyzed by x-ray diffraction method. The color of films were analyzed by CIE-L*a*b* measurement. The morphology and hardness were characterized using SEM and nano-indentation respectively. The results revealed that all ZrN thin film showed color shade in yellow gold obtained from deposition conditions of the flow rate of nitrogen 50-250 sccm, the input voltage 250-550 V, deposition time of 5-25 minutes and percent of duty cycle in rang of 30%-70%. However, in this work we found two optimum conditions. The first condition is the flow rate of nitrogen of 250 sccm, input voltage 450 V, 50% of duty cycle with deposition time of 15 minutes. The ZrN films presented by using the 1st condition showed that the hardness of films were 15 GPa, brightness 77.2%, The red rate – 2.3%, the yellow rate 24.96% in CIE-L*a*b*. The second condition is the flow rate of nitrogen 250 sccm, input voltage 350 V, 50% of duty cycle and deposition time 25 minutes. The ZrN films grown by 2nd condition shows the hardness of 15.04 GPa, the brigthtness of 68.2%, the red rate – 2.3%, the yellow 24.96% in CIE-L*a*b* condition.

Keywords: Cathodic arc, Nano-indentation, Duty cycle, Deposition time

Introduction

Nowadays the hard coating has a tremendous development of cutting tools and components such as drill bits, the tapping [2], and each one has embraced thin film coating to make is the jewelry industry surface coating. The surface coating is widely used to make hard coatings that are transition metal nitride such as zirconium nitride because the properties of zirconium nitride are given: (1) high hardness in the hard coating [2], (2) resistant to scratch or abrade well [2], (3) chemically stable [1], (4) resistant to decay, erode and impact [2] and (5) color of the hard coating similar to gold [2].

There are a number of techniques to make the hard coating zirconium nitride such as sputtering, ion beam gatorade bearing plate etc.

This research has applied coating with cathodic arc and we would study about the influence of parameters on the hardness and color of the thin film coated zirconium nitrite that enamel and decorate pieces with cathodic arc method.

Materials and Methods

Preparation the substrates

Substrate (stainless steel No. 316L) must be remove dirt and stains from grease, dust, fingerprints. To begin from the substrate have dipped in a mixture of ultrasonic cleaner 33 for 10 minutes then washed with water 4 times to clear cleaner 33 out. After that the substrate have dipped in sulfuric acid for 10 minutes then washed with water 4 times to clear sulfuric acid out. And it must dip in 100 Celsius of water for control the temperature of the substrate, blowed until dry with hairdryer, steam in a microwave to make vaporated finally**.**

Coating under conditions various

The thin film coating zirconium nitrite by cathodic arc has coated with a Physical Vapor Deposition (PVD) machine of Dongguan Huicheng Vacuum Technology JTL1110 model beneath condition.

Table 1 The study of quantity input voltage to the substrate that affect to thin films.

Data Types	Range of control
Base Pressure	1.2×10^{-2} Pa
Operating Pressure	1.5×10^{-1} - 2.5×10^{-1} Pa
Flow rate of argon (Ar)	20 sccm
Flow rate of nitrogen (N_2)	250 sccm
The electricity input to target	100 A
The input voltage to the substrate.	250 , 350, 450 and 550 volt
Percentage of duty cycle	50 %
Temperature	100-180 Celsius
	15 minutes
Deposition time	(Coating Zr 2 minutes, Coating ZrN 13 minutes)

Table 2 The study of deposition times to the substrate that affects thin films.

Data Types	Range of control
Base Pressure	1.2×10^{-2} Pa
Operating Pressure	1.5×10^{-1} - 2.5×10^{-1} Pa
Flow rate of argon (Ar)	20 sccm
Flow rate of nitrogen (N_2)	250 sccm
The electricity input to target	100 ampere
The input voltage to the substrate.	350 volt
Percentage of duty cycle	50 %
Temperature	100-180 Celsius
	5,15,25 minutes
Deposition time	(Coating Zr 2 minutes, Coating ZrN 3,13,23

Measuring instrument analyzed the unique of thin films

When the zirconium nitride thin film has coated on various conditions. It will be analyzed individual and properties. The crystal structure of zirconium nitrite thin film was analyzed by diffraction x-rays of Bruker AXS D8 discover model and was measured at incident beam 2 degree theta, range 20-80 degree theta after that we would study surface and thickness of the thin film by field emission scanning electron microscope (FE-SEM), JSM-6610LV model, the hardness of the thin film was measured by Nano-Indentator,CSM model that was compressed by berkovich. (The model look like pyramid of three side-by-side at an angle equal to 142.30 degree theta.) , the color was measured by colorimeter spectrophotometer of hunter lab, color quest XE model that radiated wavelength range 360-750 nm and can measure the color in transmission and reflection mode. In this research used a reflection mode, the light has processed with Hunter Lab program. The values are expressed in the form of hunter color index system 3 variants or CIE L*a*b*

Results and Discussion

The influence of electric potential to the substrate

The differentiation of electric potential to the substrate bias in cathodic arc can affect to thin film because when increasing electric potential, ion energy will higher and the crystal structure, color and hardness of thin film had changed.

Structure and Morphology

The results of analyzed crystal structure of thin film by x-ray diffractometer. (Figure 1) found that diffraction pattern was shown in plane (111), (200), (220) and (311) at angle 33.89, 39.329, 56.835 and 67.852 degree theta respectively. (Ref. JCPDS No.035-0753) but it didn't show in plane (222) at 71.314 degree theta due to the plane (222) had low energy of surface. The increasing electric potential made higher intensity peak of x-ray diffraction at plane (111) in each voltage but at V_b=550 volt, the intensity of x-ray diffraction at plane (111) and crystal structure had decreased because the particle of target had high energy and collided with film made lot of porouses. It called 'Resputtering'.
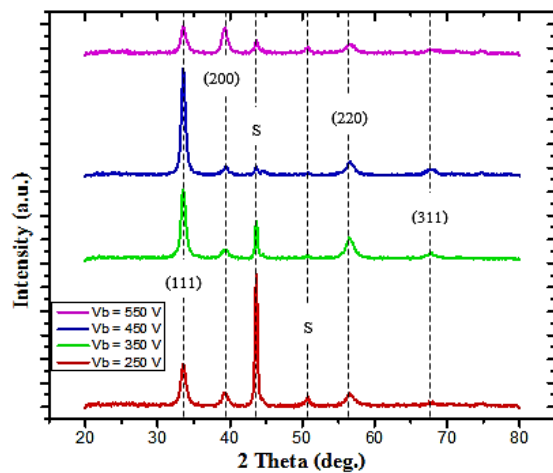
Figure 1 The result diffraction pattern of X-Ray under bias voltage conditions various.

The measurement surface characteristics of zirconium nitride thin films in figure 2 by SEM showed that zirconium nitride thin film had mostly smooth because when increasing electric potential, ion energy would

higher but it might have a little scratch on surface due to it was cleaned and polished surface before.
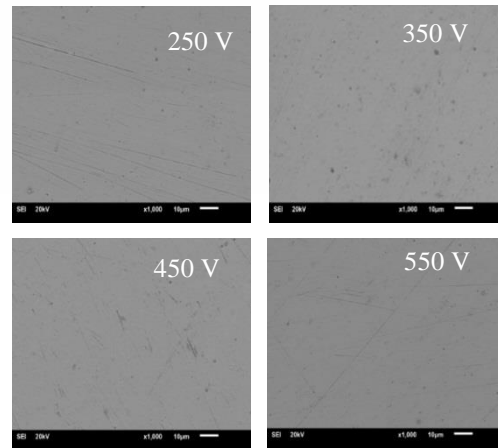
Figure 2 Expression the surface of zirconium nitride thin films each bias voltage input to the substrate

Hardness

We tested the hardness of ZrN thin film by nano-indentator found that when increasing electric potential since 250-550 volts the hardness would increase but at 550 volts the hardness had decreased due to the ZrN had lost of crystallize. We could see at plane (200) increased but at plane (111) decreased. From researching found that the hardness of ZrN at plane (111) had a hardness more than at plane (200) [2, 3].
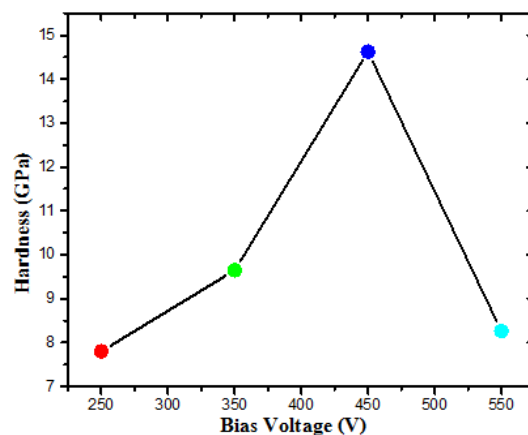
Figure 3 The relation between the bias voltages with the hardness of the film.

Optical properties

When we examined a color on surface found that the surface had like gold light but intensity of gold light was different. When increasing electric potential and analyzed a color in CIE L*a*b* system found that it had high yellowness was shown in Figures 4 and 5 respectively but redness and brightness not variable and when increasing at 450-550 volts found that yellowness had decreased due to not crystallize.
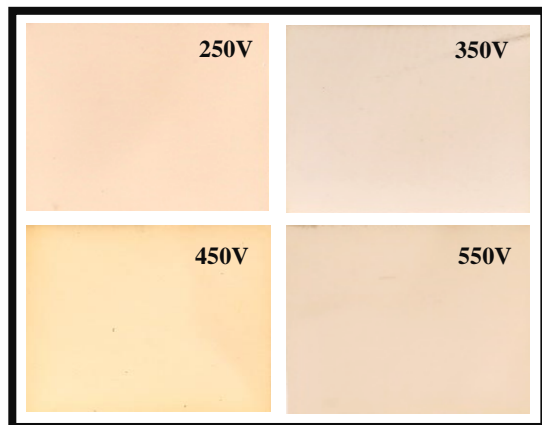

Figure 4 The color of the film on the substrate to input bias voltage on the substrate various
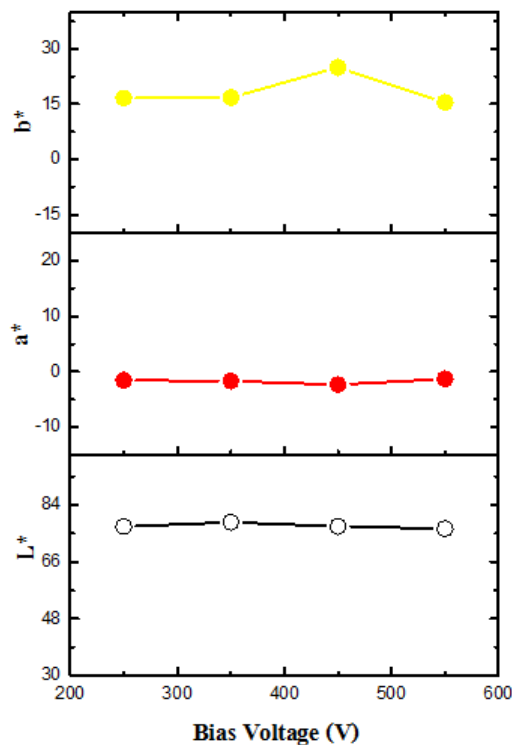
Figure 5 The relation between the yellowness (b*) redness (a*) and brightness (L*) with bias voltage to the substrate different.

Thickness

The measurement thickness of the ZrN thin film by SEM found that the thickness in range 250-350 volts had increased due to ion from target obtained energy from increasing bias voltage on the substrate in the other hand when increasing bias voltage in 350-450 volts, the thickness had decreased due to density, crystallization, hardness and yellowness of thin film had increased but at V_b = 550 volts found that the thickness had increased due to it lost of crystallize.
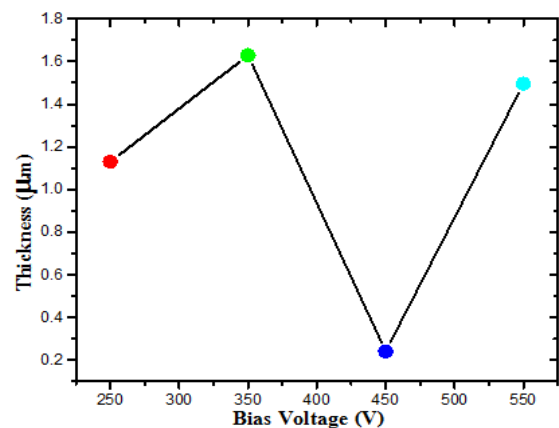
Figure 6 The relation between the thicknesses of zirconium nitride thin films with the bias voltage of the film.

The influence of deposition times

The film coating for industry, when the film thickness is increased, thus increasing the cost of production. So this experiment therefore adjust the deposition times. Which deposition times to affect directly on the thickness of films and the study influenced of deposition time on the properties of the film for developed in the industry films coating.

Structure and morphology

The measurement of X-ray diffraction the zirconium nitride coating in different conditions (Figure. 7) found that at 5 and 15 minutes. It also appeared on the substrate, but at 25 minutes. It appeared at plane (111), (200), (220) and (311). Which was completely crystalize of zirconium nitride thin film.
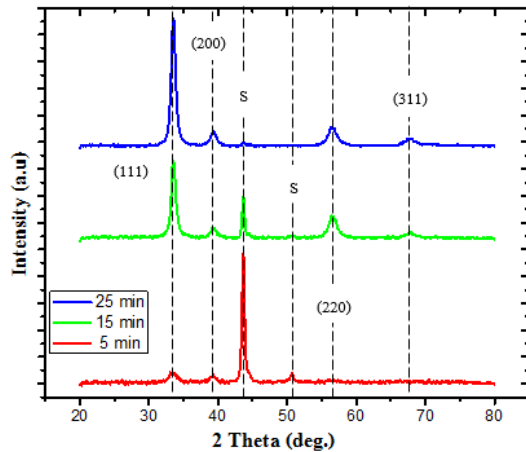
Figure 7 The result diffraction pattern of X-Ray under deposition times conditions various.

To examine surface characteristics of ZrN thin film in different times (Figure 8) found that when extending a deposit time affect to amount of grains because it accumulated lots of heat energy and the coating combined, resulting in a larger grains.
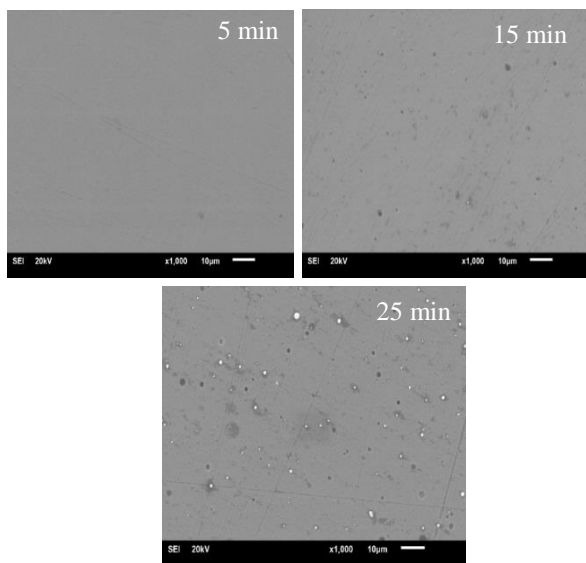

Figure 8 Expression the surface of zirconium nitride thin films each deposition times

Optical Properties

The ZrN thin film had shown a bright gold light , but when extending a deposition time   affect to intensity of bright gold increased too (figure9). However we analyzed color in CIE L*a*b* system (Figure 10) found that when extending a deposit time affects to a brightness had decreased but a yellowness had increased.
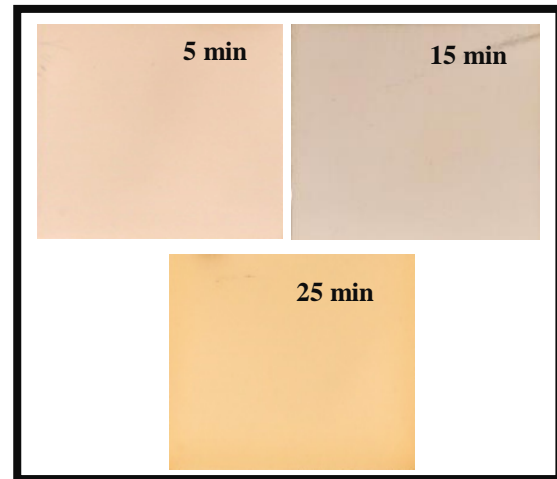
Figure 9 The color of the films to deposition times various.
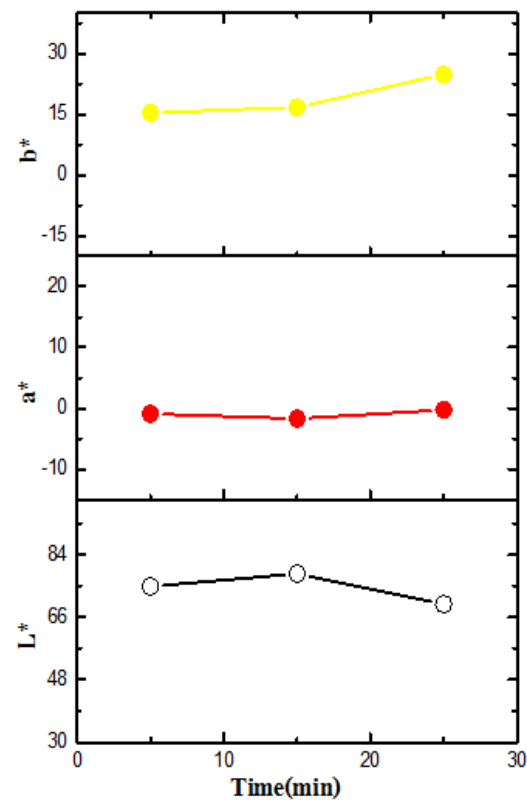
Figure 10 The relation between the yellowness (b*) redness (a*) and brightness (L*) with deposition times different.

Hardness

When extending a deposition time affect to the crystallization and hardness of ZrN thin film has increased too as a result of the arrangement of crystals at plane (111) was better (Figure 11).
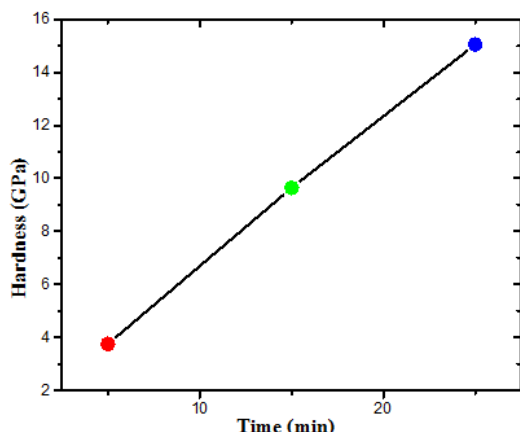
Figure 11 The relation between deposition times with the hardness of the film.

Thickness

The measurement thickness of the ZrN thin film by SEM found that when changing a deposition time affect to the thickness in linearly. We could see brightness had decreased but yellowness had increased look like gold. Another when extending a deposition time affects to the crystallization and thickness of ZrN thin film has increased too.
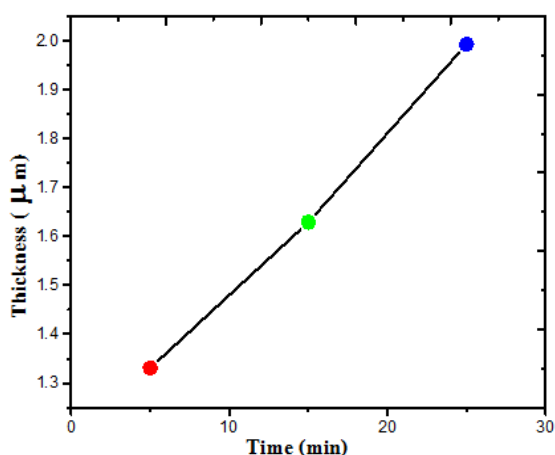

Figure 12 The relation between the thickness of zirconium nitride thin films with deposition times various.

Conclusions

The results of adjusting voltage to the substrate at 250-550 volts found that the ZrN could show a crystal structure at plane (111), (200), (220) and (311) in all of the electric potential. The film has more yellowness until V_b = 450 volt showed the highest yellowness. At the same

potential has the highest hardness at 15 GPa but the thickness has the lowest at 240 nm due to is a high pack cubic can affect to density of film higher. To study the various of thickness that affect to different color and hardness. In deposition time since 5-25 minutes when increasing the duration of coating found that the thickness has increased. The zirconium nitride thin films can show the crystal structure at plane (111), (200), (220) and (311). Meanwhile, the optical properties of thin films have decreased, but yellowness and hardness have increased. The zirconium nitride thin films which preparing with cathodic arc technique in condition V_b=450 volt, 50% duty cycle, 250 sccm flow rate of nitrogen and 25 minutes deposition time show that the film has the second hardness which is a dark golden brown.

Acknowledgement

References

[1] Mano Valaiauksornlikit, 2012, **Study of Mechanical, Optical and Electrical Properties ZrN Films by Reactive DC Magnetron Sputtering for Hard Coating Application,** A Thesis the Degree of Master of Science Program in Physics King Mongkut's University of Technology Thonburi, Page 29-85.

[2] Piolloud, D.,Dehlinger, A.S., Pierson, J.F., Roman, A.and Pichon, L., 2003, "Reactively Sputtered Zirconium Nitride Coatings: Structural, Mechanical, Optical and Electrical Characteristics", **Surface and Coatings Technology**, Vol. 174-175, pp.338-344

[3] Carvalho, P., Vaz, F., Rebouta, L., Cunha, L., Tavares, C.J., Moura, C., Alves, E., Cavaleiro, A., Goudeau, Ph., Bourhis, E.L, Rivière, J.P., Pierson, F.J. and Banakh, O., 2005, "Structural, Electrical, Optical, and

Mechanical Characterizations of Decorative ZrO_xN_y Thin Films", **Journal of Applied Physics**, Vol. 98, No. 2, pp. 715-723

[4] Milton Ohring, 2002, Material Science of Thin Films, 2ndEdition, Academic Press, London, pp.260

[5] Jirawan Saenton, 2009, **Growth of Multifuntional Zircornium Nitride Thin Films by Reactive DC Magnetron Sputtering,** A Thesis the Degree of Master of Science Program in Physics Chulalongkorn University, Page 17-45.

[6] Niu, E.W., Chen, H., Feng, W.R., Fan, S.H., Yang, S.Z. and Yang, X.Z., 2007, "Influence of Substrate Bias on the Structure and Properties of ZrN Deposition by Cathodic Vacuum Arc", **Material Science and Engineering**, Vol. 460-461, pp. 135-139.

[7] Huang, J.H., Yang, H.C., Guo, X.J. and Yu, G.P., 2005, "Effect of Thin Film Thickness on the Structure and Properties of Nanocrystalline ZrN Thin Film by Ion Plating", **Surface and Coating Technology**, Vol. 195, No. 2-3, pp. 204-213

[8] Akash Singh, P. Kuppusami, Shabana Khan, C. Sudha, R. Thirumurugesanb, R. Ramaseshan, R. Divakar, E. Mohandas and S. Dash, 2013, "Influence of Nitrogen Flow Rate on Microstructural and Nanomechanical Properties of Zr–N Thin Films Prepared by Pulsed DC Magnetron Sputtering", **Applied Surface Science,** Vol. 280**,** pp.117-123

[9] Benia, H.M., Guemmaz, M., Schmerber, G., Mosser, A. and Parlebas, J.C., 2002, "Investigation on Non-Stoichiometric Zirconium Nitrides", **Applied Surface Science**, Vol. 200, No. 1-4, pp. 231-238

Analysis of Io's Magnetic Footprint Features Using VIPAL Magnetic Field Model

C. Sukollapun[1*] and S. Wannawichian[1,2]

[1]Department of Physics and Materials Science, Faculty of Science, Chiang Mai University, Chiang Mai, Thailand

[2]National Astronomical Research Institute of Thailand *(*NARIT*)*, Chiang Mai, Thailand

* E-mail*:* enigma_thecode@hotmail.com

Abstract

Jupiter is the most gigantic planet in the solar system and generating the most intense and large magnetosphere. VIPAL magnetic field model is chosen to simulate Jupiter's magnetic field model. VIPAL was constructed based on observations by Pioneer and Voyager spacecrafts. This model appears to have a lot of benefits. For example, it can be used to analyze auroral emission in Jupiter's ionosphere. This model also has the best prediction of contact positions between ionosphere and magnetic field lines that cross Io, called Io's footprint. VIPAL also gives better magnetic field strength prediction than previous models. In order to predict footprint positions in both north and south hemispheres, we traced along the magnetic field lines beginning from Io orbital position to the footprint locations in ionosphere. There are many factors to be considered, for example, the shape of Jupiter, Io's orbit inclination and eccentricity, to get the best prediction of footprint position as possible. These positions are expected to have the emission of auroral features. One of the most important of this features are their brightness. Previous studies found that this brightness has a strong relation with Io longitude and relates to the latitude of Io in the torus. Therefore, in order to make better physical interpretation, the relation between Io footprint brightness and magnetic field strength is presented in this work.

Keywords: Jupiter, VIPAL, Io, Footprint, Aurora

Introduction

Jupiter has the most extreme planetary magnetic field in our solar system. This magnetic field generates an enormous magnetosphere around the planet, which internal plasma and satellites interact. Study of magnetosphere and its consequences will be beneficial in Astrophysics.

Currents from the interaction between plasma and satellites follow the magnetic field lines and fall into the Jovian ionosphere. These currents collide with Jupiter atmospheric particles, which emit auroral emission. One of the most intense aurora emission comes from the interaction between Io, one of Galilean satellite, and magnetosphere. In order to predict Io footprint positions in both north and south hemispheres, we traced along the magnetic field lines beginning from Io orbital position to the footprint locations in ionosphere via Jovian magnetic field model.

Model of magnetosphere is used to determine magnetic field strength and the direction of magnetic field lines around magnetized object. There are many models of Jupiter's magnetosphere. Each model varies depending on the method and constraints used to construct.

Materials and Methods

The right magnetic field model is chosen from three models which are VIP4 (Voyager, Io footprint, Pioneer observations and the maximum degree and order fourth of the fit model [1], VIPAL (Voyager, Io footprint, Pioneer observations and the modeling of the lowest orders of the magnetic anomaly and corrects for the longitudinal position of the magnetic field line mapping to Io's orbit) [2] and the

last model; GAM (Grodent anomaly model) [3,4]. VIPAL is an update version of VIP4 and has more coefficients up to fifth order.

VIPAL has the best footprint prediction for magnetic field in the northern hemisphere with mean spherical difference between observed and model footpath 3.31°. While GAM and VIP4 has the differences 3.52° and 5.04°, respectively. In the southern hemisphere GAM is not applicable and VIP4 has the best fitting of footpath with mean spherical difference between observed and model footpath 2.33° compared with VIPAL which has the difference 3.27° [3,4]. In order to choose between VIP4 and VIPAL we considered mean spherical difference in both north and south hemispheres. VIPAL has the average mean spherical difference at 3.29°, compared with VIP4 which has 3.685°. We conclude that we should use VIPAL because this model has better prediction.

The magnetic field model was used to trace down the magnetic field line that pass Io orbit to Jupiter Ionosphere, which is expected to be auroral positions. First, we choose any position in the magnetosphere. Next the magnetic field strength at that position in three coordinates, was calculated by VIPAL magnetic field model. From the magnetic field strength in each three directions, we can determine the direction of magnetic field and move along this direction a little to a new location. By iteration this procedure, the magnetic field line can be traced. In the case of Io, we traced from Io position at 5.9 RJ along both north and south hemispheres, resulting in footpaths in both north and south polar regions.

The data from magnetic field model is analyzed by combining with observation data obtained from Advanced Camera for Surveys (ACS) operating on Hubble Space Telescope (HST). In the end, we will have four information which are magnetic field strength and footprint brightness for both north and south hemispheres. By combining this data, more behavior of aurora and magnetic field strength will be interpreted in the next session.

Results and Discussion

Magnetic field strength at Io footprint between north and south hemisphere

There are significant differences in magnetic field strength in both north and south hemispheres at the same longitude as seen in Figure 1. In addition, the trend of magnetic variation in both hemispheres does not correlate with each other as well. For example, the decreasing of magnetic field strength in north hemisphere begin around 150° longitude, in contrast with the decreasing magnetic field strength in south hemisphere. The maximum value of magnetic field strength differs around 5 gauss but the minimum is roughly the same. As a result, for magnetic field line passing Io (at the same longitude), the positions of magnetic footprints in both hemispheres should not be the same as well as magnetic field strength. Therefore, this result may be effected by physical shape of Jupiter, plasma travel time along magnetic field line and lead angle that comes from Io torus. Further study may help evaluate these hypotheses.

Io footprint brightness in north and south polar regions

The brightness of magnetic field footprint is obtained from north and south polar regions separately, as seen in Figure 2. It must be noted that, at time, we can obtain images only for north or south aurora in specific Io longitude and time. Combination data from both hemispheres show peak brightness around 110° and 270° Io longitudes [5]. Although, there is huge discontinuity of footprint brightness around 110° Io longitude between both hemispheres.

Relation between brightness and magnetic field strength of both hemispheres

There is intriguing relation between magnetic field strength and footprint brightness because the variation trends of both values are not dependent to each other as seen in Figure 3. There are other factors that we need to take into consideration. It is possible for the fact that the magnetic field strength does not influence the footprint

brightness directly. However, we should expect slight relation from both factors, considering the more photon numbers penetration (more brightness) should relate to the less magnetic field strength. Moreover, additional footprint brightness data must be obtained, such as completed data in 360° Io longitude for both hemispheres, in order to increase analyzing ability. Table 1 shows comparison between magnetic field strength and footprint brightness of a few overlapping points around 110° both north and south hemispheres.
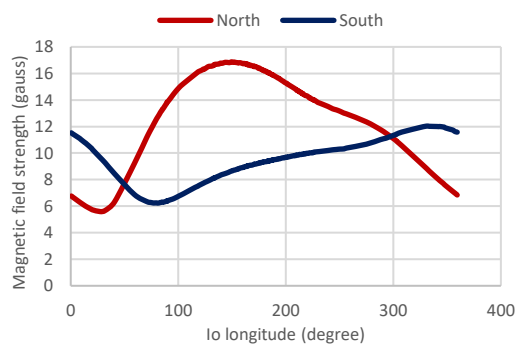
Figure 1 shows magnetic field strength at Io footprint position in both north and south hemispheres.
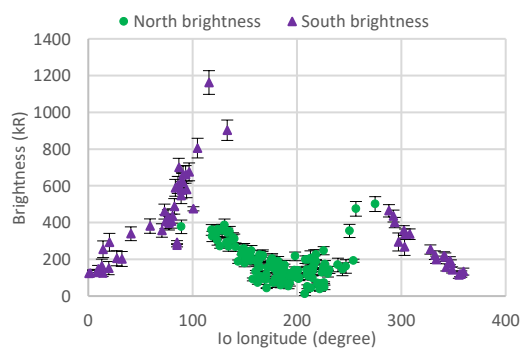
Figure 2 shows Io footprint brightness in both north and south hemispheres.
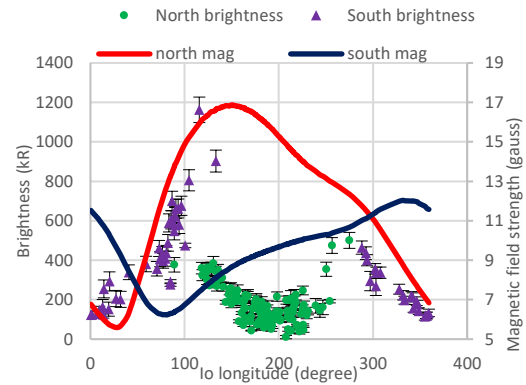
Figure 3 shows combination of Io footprint brightness and magnetic field strength in both north and south hemispheres.

Table 1 shows comparison between magnetic field strength and footprint brightness of six overlapping points around 110° both north and south hemispheres.

North			South		
Io Longitude (degree)	Magnetic Field Strength (gauss)	Brightness (kR)*	Io Longitude (degree)	Magnetic field strength (gauss)	Brightness (kR)*
89.12	13.77	376.96	89.11	6.38	547.27
118.31	16.116	359.96	115.65	7.41	1162.37
133.16	16.65	343.88	133.19	8.10	902.62

*1 kR = 10^9 photon $cm^{-2}s^{-1}$ into 4π steradians [5]

Conclusions

At the same Io longitude, magnetic field strength is different in both north and south hemispheres. In addition, their trend does not correlate with each other across 360° Io's longitude. While, the observed magnetic footprint brightness has two peak brightness around 110° and 270°, however, there is discontinuity around 110°. The relation between magnetic field strength and footprint brightness should be further investigated, while other factors are well controlled.

References

[1] Connerney, J. E. P., Acuña, M. H., Ness, N.F., and Satoh, T. 1998. "New models of Jupiter's magnetic field constrained by the Io flux tube footprint". **Journal of Geophysical Research**. 103(A6): 11,929–11,939.

[2] Hess, S. L. G., Bonfold, B., Zarka, P., and Grodent, D. 2011. "Model of the Jovian magnetic field topology constrained by the Io auroral emissions". **Journal of Geophysical Research**. 116: 5,217-5,236.

[3] Vogt, M. F., Kivelson, M. G., Khurana, K. K., Walker, R. J., Bonfond, B., Grodent, D., and Radioti A. 2011. "Improved mapping of Jupiter's auroral features to magnetospheric". **J. Geophys. Res.** 116: A03220.

[4] Vogt, M. F., Bunce J., Kivelson, M. G., Khurana, K. K., Walker, R. J., Radioti, A., Bonfond, B., and Grodent, D. 2015. "Magnetosphere-ionosphere mapping at Jupiter: Quantifying the effects of using different internal field models". **Journal of Geophysical Research: Space Physics**.120(4): 2,584-2,599.

[5] Wannawichian, S., Clarke, J. T., and Nichols, J. D. 2010. "Ten years of Hubble Space Telescope observations of the variation of the Jovian satellites' auroral footprint brightness". **Journal of Geophysical Research**. 115(A2): 2,206-2,214.

Solar and Lunar Eclipses Modeling by Using Minecraft for Elementary Students

S. Nutaro[1*], S. Yingphaiboonsuk, T. Rodhiran, N. Seemanta, C. Junngam and W. Siripee[2]

[1]Department of Elementary Education, Faculty of Educaton, Ubon Ratchathani Rajabhat University,

2 Chang Sanit Road, Tambon Nai Muang, Amphur Muang, Ubon Ratchathani, 34000

[2]The Laboratory school of Ubon Ratchathani Rajabhat University,

2 Chang Sanit Road, Tambon Nai Muang, Amphur Muang, Ubon Ratchathani, 34000

*E-mail: sukanya.vi@ubru.ac.th

Abstract

Solar and lunar eclipses are astronomical phenomena that is an excellent topic for introducing astronomy to primary school students. We have used Minecraft, which is a popular game about placing blocks to construct virtual environment, and can make a simple model of the Sun, Moon and Earth easily. The background knowledge of Pratom 6 students (grade 6) has already had about the position of them on Earth and how they see the Sun and Moon. This article will show how students investigate the relationship between Sun, Moon and Earth and when will solar and lunar eclipses occur in their game situation. After class students should draw and write essay about solar and lunar eclipses concept paper. The results show that collaborative learning by using Minecraft is effective to students, 81% of students could write and draw the correct science concept of solar and lunar eclipses, 14% of students could only write and draw about the position of each planets when solar and lunar eclipses happen and 5% of students could not write anything about solar and lunar eclipses but he explained how to make 3 spheres as well. A large majority of students, 90%, reported enjoying using Minecraft and wanted to see Minecraft used in the classroom again.

Keywords: Minecraft, Game-based learning, Solar and lunar eclipses concept, Collaborative learning

Introduction

Similar initiatives on curriculum reform in several countries have set ambitious goals to increase scientific literacy among the population because science and technology can make a new world which is coming soon. Science in primary classroom affected a powerful of basic science concept in our students' life. Lightman and Sadler [3] found that students in grades 8 to 12 shared some of the conceptions held by elementary school children. Though more than 60% of the students held the accepted scientific concept about the day-night cycle, less than 40% knew the correct characteristics of the Moon's revolution. Furthermore, less than 30% had the right conception about the phases of the Moon, the Sun overhead and the Earth's diameter, and only 10% knew the reason for the change of seasons. Solar and lunar eclipses are astronomical phenomena that these contents are in grade 6 of science curriculum of Thailand, the students will investigate and understand the relationships among the earth, moon, and sun.

Minecraft is a sandbox building video game written in Java and published by the company Mojang. It was released in May 2009 on the home computer platforms with an Apple IOS and Android in 2012 system. The game play is centered on creativity and building, with players building (crafting) constructions out of textured cubes in a 3-dimensional world [2]. Some players and developers argue that video games are better at teaching logic and problem solving skills

than many school curriculums. Some game has adopted aspects that are defined to be similar or base on scientific implementation. Minecraft is one of the games with such aspects [4]. It was chosen to be a tool of learning in solar and lunar eclipses with 6 grade students, 21 students of Ban Hnong Khainok school. Using Minecraft to model solar and lunar eclipses from the knowledge in science classroom.

Materials and Methods

After students learned regular science lesson in classroom in the contents of solar and lunar eclipses. Minecraft (Figure 1) was used to be the tool to model the solar and lunar eclipses of the 6 grade students at Ban Hnong Khainok school, Ubon Ratchathani, Thailand.

Figure 1 Minecraft, which is an openly free formed game.

The participants in this study were students chosen by purposive sampling. Researchers used non-experimental research design which is case study design. Students were provided with a set of step-by-step instructions detailing how to using Minecraft. Then they worked in group of 7 students collaborate to build their solar and lunar eclipses model. Then they drew and wrote essay about solar and lunar eclipses concept paper.

Table 1 Program of Minecraft lessons implemented at Ban Hnong Khainok school to assist in teaching grade 6 solar and lunar eclipses.

Week	Title of Lesson	Time allocated (Minutes)
1	Regular learning in solar and lunar eclipses	100
2	Introduction and how to use Minecraft	100
3	Design and build	250
4	Drawing and writing	

Results and Discussion

All the group of student can build spheres which were used to be sun, moon and earth but they did not use the scientific fact of size and distance among each spheres (Figure 2). With our sample of experiment group, they can understand clearly about the position of each planets, and choose point of view to observe the phenomena in their virtual environment (Figure 3). One group tried to make a shadow on the surface of the sphere to explain what could we see when solar and lunar eclipses happen (Figure 4).

Figure 2 Model of the Sun, Earth and Moon created by students.

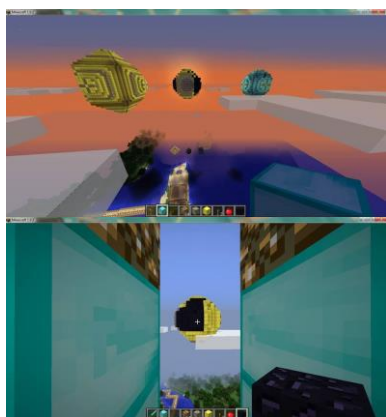**Figure 3** One of the points of view which students observed.

Figure 4 Screenshots showing students were making a shadow of the sun by using the dark material.

In their essays, 81% of students could write and draw the correct science concept of solar and lunar eclipses, 14% of students could only write and draw about the position of each planets when solar and lunar eclipses happen and 5% of students could not write anything about solar and lunar eclipses but he explained how to make 3 spheres as well. A large majority of students, 90%, reported enjoying using Minecraft and wanted to see Minecraft used in the classroom again.

For these content, solar and lunar eclipses, there are some obstacle with using Minecraft because students can not simulate the animation of the movement of each spheres so they did the 2 models, solar eclipses and lunar eclipses separately from each other.

Conclusions

The Minecraft activities were designed to use a number of higher-order thinking skills represented in Bloom's revised taxonomy [1]. In our research, students created a structure using their current understandings to astronomical phenomena, solar and lunar eclipses. For some students who used to play it and were already familiar with Minecraft were observed helping less experienced students.

A Minecraft can be designed by the teacher who would like to present a tool to benefit the learning process of students in scientific or social way. It has been used throughout the world to represent scientific concept.

References

[1] Churches, A. 2009. "Bloom's Digital Taxonomy".
    Retrieved from Educational Origami:
    http://edorigami.wikispaces.com/Bloom%27s+Dig
    ital+Taxonomy

[2] Daniel Short. 2012. "Teaching Scientific Concepts
    using a Virtual World - Minecraft".
    Teaching science. 58(3), 55-58.

[3] Lightman, A. & Sadler, P. 1993. "Teacher
    predictions versus actual student gains".
    The Physics Teacher. 31, 162–167.

 [4] Glenn Ekaputra, Charles Lim, Kho I. Eng. 2013.
    "Minecraft: A Game as an Education and
    Scientific Learning Tool". **Proceeding of
    Information Systems International Conference
    (ISICO)**, 237-242.

Earth's Auroral Activity at Polar Region in Responding to Solar Wind Dynamic

P. Jamlongkul[1*] and S. Wannawichian[1,2]**

[1]Department of Physics and Materials Science, Faculty of Science, Chiang Mai University, Chiang Mai 50200, Thailand

[2]National Astronomical Research Institute of Thailand (NARIT), Chiang Mai 50200, Thailand

* E-mail: Paparin.jamlongkul@gmail.com

** E-mail: Suwichawan@gmail.com

Abstract

The occurrence region of the Earth's aurora is mostly near the pole. The terrestrial aurora has a feature of emission band, which locates around geomagnetic latitude between 61 and 73 degrees. The appearance of the aurora is not in a stable form but changing with time. This study presents 5 periods of Earth's auroral activity on April 28, 2007, which was observed by the Visible Imaging System (VIS) cameras on board POLAR spacecraft. The image size was taken in 12s exposure time during the Global Geospace Science (GGS) program. The analysis of auroral activity shows that the brightening zone of the auroral oval changes with various time scales. To compare with the model of auroral activity over the entire polar region, there are two characteristic phases around 2-3 hours, an expansive phase and a recovery phase. In addition, the solar wind data, which are Interplanetary Magnetic Field (IMF), solar wind plasma speed, and solar wind proton density will be used to determine the corresponding of auroral activity to solar wind dynamic in each phase. From this study, the various cases of terrestrial auroral activity will be presented.

Keywords: Auroral activity, Solar wind dynamic

Introduction

The Earth's aurorae, the Northern and Southern lights, are caused by interaction between charged particles (electron and positive ions) from the solar wind which are trapped in the Earth's magnetic field and gas molecules such as oxygen and nitrogen at the Earth's ionosphere. Earth is believed to be similar to a large dipole surrounded by magnetic field which is strongest at the pole regions and reduces in further distance from the polar regions. When the solar wind, high speed particles originated from the sun, interacts with Earth's magnetic field, the field configuration changes into a teardrop-like shape [1]. The compressed field in sunward direction is called the dayside magnetosphere and the stretched field in anti-sunward direction is called the magnetotail [2]. The solar particles could penetrate into Earth's magnetosphere by reconnection, the merging between the solar wind and the Earth's magnetic field, and move along the magnetic field lines toward to the Earth's poles creating an elective volt between magnetotail and poles. Because of the voltage occurred by build-up pressure from the solar wind, the high energy solar particles (mostly electrons) precipitate into the Earth's ionosphere, the upper layer of the atmosphere, and collide with the neutral molecules in ionosphere. After colliding, the excited electrons bound by the neutral molecules return to lower energy state and finally release the photons in several frequencies. Earth's aurora can be many colors depending on the type of the gases: greenish-yellow or bloody-red light from oxygen and blue light from nitrogen (rare occasion, approximately once every 10 years) [1,3]. The shape of the aurora depends on the location in the magnetosphere that the electrons came from and the process that drives them into the atmosphere. The aurora features basically remain fixed as oval band which is called

the center of auroral oval locates off the pole around 3 or 4 degrees and sweeps out around geomagnetic latitude between 61 and 73 degrees [1].

The appearance of the aurora is not the fixed pattern, but changing with time. A sequence of simultaneous auroral events over the entire polar region from auroral quiet through the active phases toward relaxation state is explained in term of an auroral substorm.

Each auroral substorm has a period of time around 1-3 hours, and comprises of 2 phases. It mostly occurs 5-6 times per day. The first phase is called the expansive phase which takes proximately 30 minutes, and is divided into 3 stages. This phase begins from the quiet phase when the aurorae are free from activity. Aurora appears quiet and homogeneous arcs. Next, the activity moves to the stage I, a sudden brightening of one of quiet arcs within a few minutes. After that, the brightening arc moves poleward and creates bulge around the midnight sector, while there is pseudo break-up which enlarges the bulge and starts moving southward around 5-10 minutes in stage II. The last stage in this phase, the stage III, when the active arc moves to south-western, the front of the expansive bulge becomes extremely intense and propagates westward, as the westward current, for approximately 10-30 minutes. In the end of this stage, the active band moves poleward or toward the arcs and the patches, which present during quiet periods. After becoming brighter, the last phase or the recovery phase which have life time around 30 minutes to 2-3 hours starts. This phase is also divided into 3 stages. First, as soon as the northernmost active band reaches its highest latitude, it starts to return southward with slower westward speed which may degenerate into irregular-shaped folds and form the well-defined loops, an important indicator of intensity of the substorm. The grow from the bulge takes around 30 minutes to 1 hour to become weaker in stage I. In the stage II, new arcs form and the patches join in the equatorward motion and disappear. However, some patches seem to converge to form the homogeneous arcs for around 1-2 hours. The final stage of the recovery phase or the stage III is also presented by slow equatorward

motion of arcs. There is not eastward or westward motion and takes 2-3 hours to be back to the quiet phase [4-5]. The phases of each auroral substrom should be mostly similar unless there are other effects. The main influence is from the solar wind. Determination of the corresponding activity for each phase can be done by considering the solar wind data which are the Interplanetary Magnetic Field (IMF), solar wind plasma speed, solar wind proton density, solar wind dynamic pressure, and Kp-index [6]. In this work, we study the phases' time scale of the auroral substorm from direct observations of auroral emission to determine the relation between the auroral activities and the solar wind activities.

Materials and Methods

Observation and Data Analysis

Images of auroral substorm were observed by the Visible Imaging System (VIS) cameras on board POLAR spacecraft. Each image was taken in 12s exposure time during the Global Geospace Science (GGS) program on April 28, 2007 [7]. The observed images were considered and chosen into 5 sets that each set presents all phases as shown in Figure 1. Next, we recorded time scale for each stage of phases and compared with the solar wind data which were obtained from the Low Resolution OMNI (LRO) data set [8], as shown in Figure 2.

Results and Discussion

We chose 5 sets of all images by considering sections of time which seemed to be covered all completed phases. Plotting physical properties of solar wind was used for comparison with its activities of each stage as shown in Table 1.

The Table 1 presents physical properties of solar wind which are used to determine the activity of each stage in 5 sets. Overall, it can be seen that the most active aurora in set 1 was corresponding to strongest solar wind physical properties above the other sets.

For set 1, aurora in the stage III is brightest as shown in Figure 3 . Accordingly, the highest BIMF, and solar wind

dynamic pressure were found in set 1, although solar wind speed and Kp-index were almost lowest.

The solar wind properties in other sets were significantly lower. BIMF in set 3 and 5 were slightly lower than set 2 and 4, and set 5 was the lowest. Solar wind dynamic pressure for set 2, 3 and 5 were comparable. As solar wind dynamic pressure depends on solar wind proton density and solar wind speed, solar wind dynamic pressure changes faster with solar wind speed square. For three sets with intermediate auroral activities, solar wind speed in set 2 and 3 were comparable but quite different from solar wind speeds in set 5, the highest to solar wind dynamic pressure which has approximately 20% above the others. Set 4 has by far the lowest solar wind physical properties in terms of solar wind dynamic pressure including solar wind proton density and solar wind speed.

The last physical properties, Kp-index, is visible scale to see the aurora [10]. There were comparable values of Kp-index for all sets which means the aurora can be seen but not necessarily be the same brightness.

The most active aurora tended to occur in the stage III of the expansive phase which had the greatest oval band of each set as shown in the Figure 3. It is determined that the maximum value of BIMF, and solar wind dynamic pressure in set 1 corresponded to the brightest band although the solar wind speed was not very fast but solar wind proton density was highest. Furthermore, the comparable sets which have slow solar wind speed appear to have little activity of aurora.
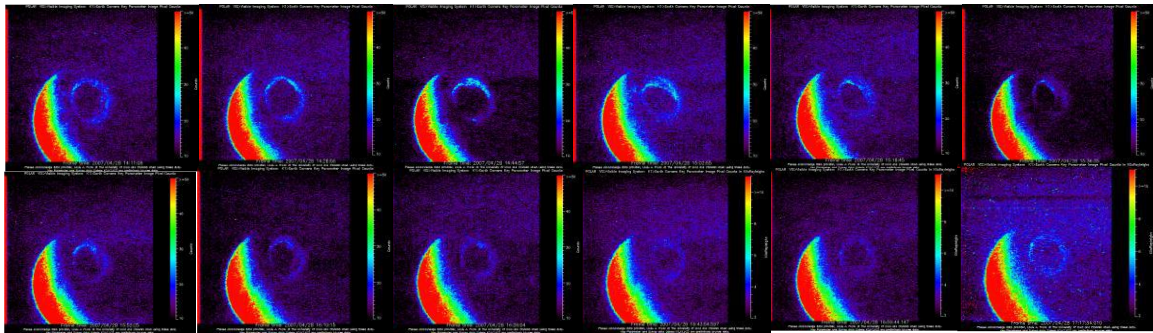
Figure 1 An example set of images shows all phases occurring on April 28, 2007 from 14:11:08 UT to 17:17:34 UT by CDA Website [9].
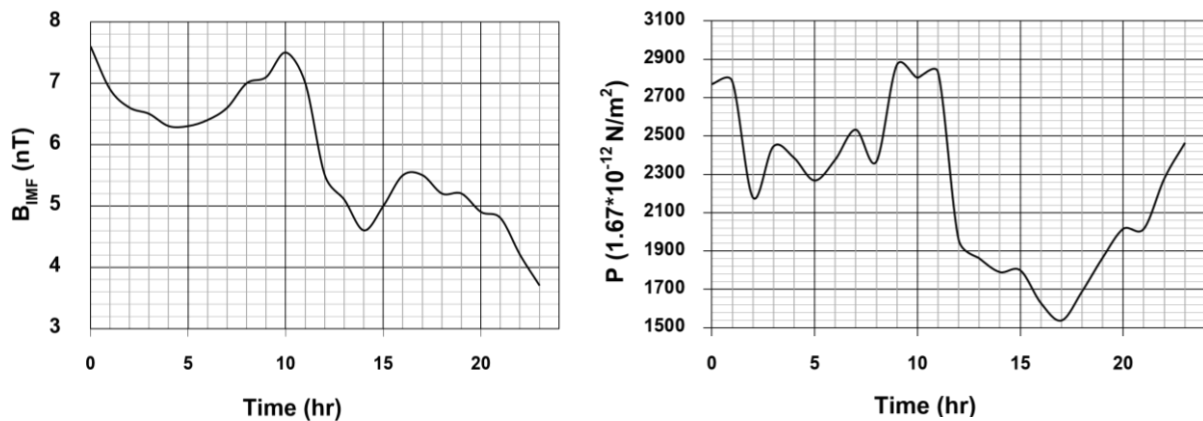
Figure 2 Examples of solar wind variability obtained from the Low Resolution OMNI (LRO) data set [8].
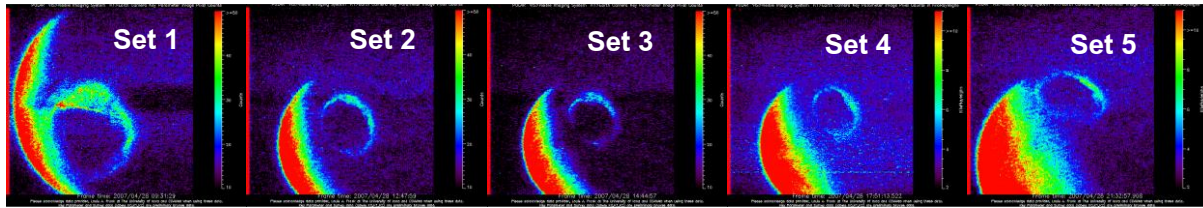
Figure 3 The stage III of the expansive phase from set 1 to 5, respectively.

Table 1 Physical properties of solar wind which are components of B_{IMF}, solar wind proton density, solar wind plasma speed, solar wind dynamic pressure, and Kp-index during the time interval of each phase.

#set	Name of Phase	Lower limit of time scale (hh:mm:ss)	Upper limit of time scale (hh mm:ss)	B_{IMF} (nT)	ρ_{sw} (N/cm^3)	V_{sw} (km/s)	Dynamic Pressure (1.67*10^{-12} N/m^2)	Kp-index
1	E I*	08:43:06	08:57:29	7.0 → 7.1	4.1 → 5.0	577 → 574	2366 → 2870	4
	E II*	08:57:29	09:31:29	7.1 → 7.5	5.0 → 4.8	574 → 584	2870 → 2803	4+
	E III*	09:31:29	09:49:22	7.1 → 7.5	5.0 → 4.8	574 → 584	2870 → 2803	4+
	R I, R II, R III**	09:49:22	11:56:30	7.5 → 7.0 → 5.5	4.8 → 4.9 → 3.3	584 → 578 → 594	2803 → 2832 → 1960	4+
2	E I	11:56:30	12:14:20	5.5 → 5.1	3.3 → 3.1	594 → 601	1960 → 1863	4
	E II	12:30:10	12:47:59	5.5 → 5.1	3.3 → 3.1	594 → 601	1960 → 1863	4
	E III	12:47:59	13:03:49	5.5 → 5.1	3.3 → 3.1	594 → 601	1960 → 1863	4
	R I, R II, R III	13:03:49	14:11:08	5.1 → 4.6	3.1 → 3.0	601 → 597	1863 → 1791	4
3	E I	14:11:08	14:28:58	4.6 → 5.0	3.0	597 → 600	1791 → 1800	4
	E II	14:28:58	14:44:57	4.6 → 5.0	3.0	597 → 600	1791 → 1800	4
	E III	14:44:57	15:02:55	4.6 → 5.0	3.0	597 → 600	1791 → 1800	4
	R I, R II, R III	15:02:55	17:17:34	5.0 → 5.5 → 5.5	3.0 → 2.8 → 2.7	600 → 582 → 570	1800 → 1630 → 1539	4-
4	E I	17:17:34	17:33:23	5.5 → 5.2	2.7 → 2.9	570 → 583	1539 → 1691	4-
	E II	17:33:23	17:51:13	5.5 → 5.2	2.7 → 2.9	570 → 583	1539 → 1691	4-
	E III	17:51:13	18:02:26	5.5 → 5.2	2.7 → 2.9	570 → 583	1539 → 1691	4-
	R I, R II, R III	18:02:26	20:41:31	5.2 → 5.2 → 4.9	2.9 → 3.1 → 3.3	583 → 602 → 611	1691 → 1866 → 2016	4-
5	E I	20:41:31	20:59:21	4.9 → 4.8	3.3	611	2016	5-
	E II	21:15:11	21:32:57	4.8 → 4.2	3.3 → 3.7	611 → 616	2016 → 2279	5-
	E III	21:32:57	21:55:42	4.8 → 4.2	3.3 → 3.7	611 → 616	2016 → 2279	5-
	R I, R II, R III	21:55:42	23:58:13	4.2 → 3.7 → 4.6	3.7 → 3.9 → 3.5	616 → 632 → 637	2279 → 2465 → 2230	4

*E stands for 'Expansive phase' which compounds of 3 stages: stage I, II, III

**R stands for Recovery phase', which compounds of 3 stages: stage I, II, III

Conclusions

From comparison between auroral images and solar wind activities, it is concluded that the solar wind dynamic pressure plays major role which can be seen in the most active expansive stage III in set 1. Nonetheless, it may be other influences such as BIMF configuration which can change auroral features and time scale of occurring auroral substorm. My future works will study the auroral feature in detail, as well as quantitatively acquire the brightness of the aurora.

References

[1] Akasofu, S.-I. 2007. **Exploring the Secrets of the Aurora: Confronting Paradigms: Aurora Research During the Early Space Age (Second Edition)**. Alaska, U.S.A.: Springer Science+Business Media, LLC.

[2] Hughes, W.J. 1995. **Introduction to Space Physics: The Magnetopause, Magnetotail, and Magnetic Reconnection**. New York, U.K.: Cambrige University Press.

[3] Carlson, Jr., Egeland, A. 1995. **Introduction to Space Physics: The Aurora and the Auroral Ionosphere**. New York, U.K.: Cambrige University Press.

[4] Akasofu, S.-I. 1964. "The Development of the Auroral Substorm". **Planet. Space Sci.** 12: 273- 282.

[5] Akasofu, S.-I., Lui, A.T.Y., and Meng, C.-I. 2010. "Importance of auroral features in the search for substorm onset processes". **J. Geophys. Res.** 115: A08218.

[6] Akasofu, S.-I. 2007. **Exploring the Secrets of the Aurora: Synthesis of Magnetospheric Substorm Phenomena (Second Edition)**. Alaska, U.S.A.: Springer Science + Business Media, LLC.

[7] Frank, L. A., *et al*. 1993. "The Visible Imaging System (VIS) for the Polar Spacecraft". **Space Sci. Revi.** 71: 297-328.

[8] NASA/GSFC's Space Physics Data Facility, http:// omniweb. gsfc.nasa.gov, March 10, 2016.

[9] NASA's Space Physics Data Facility, ftp://cdaweb.gsfc. nasa.gov/pub/data/polar/vis/vis_earth-camera-full/, March 10, 2016.

[10] Levitin, A.E., Gromova, L.I., Gromov, S.V., Dremukhina, L.A. 2012. "Kp-index and Local High-Latitudeinal Geomagnetic Activity". **Proceedings of the 9th Intl Conf. "Problems of Geocosmos".** pp. 295-301.

Application of Tritium and Stable Isotope as the Tracers on Groundwater and Reservoir Leakage Study of Limestone Aquifer in Chiang Dao Area, Northern Thailand

C. Saengkorakot[*], M. Yongprawat, W. Kunsawat, B. Porntepkasemsan and N. Noipow

Nuclear Research and Development Division, Thailand Institute of Nuclear Technology (Public Organization)

Ongkarak, Nakorn Nayok 26120

*E-mail: chakrit@tint.or.th

Abstract

The groundwater in Chiang Dao Area, Chiang Mai province is geologically related to limestone, which exposed as beautiful Karst topography. The groundwater system in Karst Area usually formed caves and underground conduits with turbulent flows and rapid vertical infiltration. The unique recharge mechanism make the aquifers tends to be complex, high heterogeneity and change in very dynamic with high surface water-groundwater interaction associate vast of springs. The reservoirs in the area usually faced of leakage problems and short of storage in dry season. The stable isotope ratios (δ^2H, $\delta^{18}O$) of 42 water samples of groundwater, surface water and springs, collected in 2013-2014, were analyzed by isotopic H_2O laser spectroscopy instrument (Picarro L2130-i) and the radionuclide Tritium content in water samples were ultra-low level measured by Liquid Scintillation Counter (LSC) with Electrolytic Enrichment. The data can be applied as environmental tracers to identify the GW recharging sources and SW-GW interaction. In surface water, the reservoir water can be separated to the streams by very high enrichment ($\delta^{18}O$>-5.0) from higher evaporation effect. The SW-GW interaction can be defined by evaporation fingerprint with $\delta^{18}O$>-7.1 in 2 groundwater wells and 5 springs that located close to the reservoirs. Tritium content in SW range from 1.8-2.3 Tritium Unit (TU) that the range can be defined as "Modern water". Tritium content in GW in the study area range from 0.3-2.0 TU, and can be divided into 2 groups. The GW in recharge area at higher altitude (>620 m above MSL.) can be interpreted as modern water recharged by Tritium content of 1.8-2.0 TU, while GW in discharge area at lower altitude (422-620 m above MSL.) can be defined as mixture of modern and sub-modern (prior 1952) GW recharged by lower Tritium content of 0.3-1.9 TU The reservoirs and GW system including springs in recharge area (altitude >620 m), which show evaporation fingerprint and "Modern water" tritium characteristic, will be defined as higher risk in short of storage or decline of water level by leakage or rapidly recharge to the lower GW water system (base flow) in the dry season.

Keywords: Stable isotope, Tritium, Groundwater, Karst, Reservoir

Introduction

The Chiang Dao Area is geologically composed of the large area of Permian limestone (Ngao Group) approximately deposited in marine environments about 250 Ma [1]. The succession mainly composed of carbonate sedimentary rocks which are soluble, which usually formed "Karst Topography" and developed beautiful landscapes associated with many caves and underground passages. The famous tourist attractions "Doi Luang Chiang Dao" and "Chiang Dao Cave" are good representative of karst landscapes in the area.

The groundwater (GW) system in karst area usually controlled by caves and well developed fracture networks called "Conduits" that make GW flow in the limestone aquifers tends to be complex, high heterogeneity and associate vast of springs. The unique turbulent flows of GW in the conduits and rapid vertical infiltration make the aquifer change in very dynamic with

The unique turbulent flows of GW in the conduits and rapid vertical infiltration make the aquifer change in very dynamic with very high surface water-groundwater interaction. [2] The development of reservoirs in the area usually faced of leakage problems and short of storage in dry season (Figure 1)

Figure 1 Huai Luek Dam, Tambon Ping Khong, Chiang Dao District in December 2013, this dam was designed as underground reservoir.

The objective of this study was characterization of recharged sources and mechanisms of the GW systems in the study area as well as the identification of GW-SW interaction by stable isotopes and radioactive isotope tritium, which is widely used as the tracers in hydrology and GW studies [3-5].

Materials and Methods

The study area is approximately 250 km^2, located in the easthern part of Chiang Dao District and southern part of Chai Prakan district (Figure 2), which was exposed by prominent limestone range at high attitude contributed the "exokarst" and characterized as the main recharge area.

The water was flow to the discharge areas in lower attitudes through the conduit networks, which frequently consist vast of spring outlets (the local name called "Nam Ru" or "Nam Phu"). The 42 water samples including reservoirs, streams, springs and GW from the local production wells, were collected in rainy season (September 2013) and dry season (April 2014). The stable isotope ratios (δ^2H, δ^{18}O) [6] were analyzed by the Cavity Ring-down Spectrometer (CRDS) isotopic H$_2$O analyzer (Picarro L2130-*i*), the analyzer based on Beer's law and non-dispersive laser absorption technique [7-8] (Figure 3), which the precisions (1σ) are better than ±0.5‰ and ±0.15‰ for δ^2H and δ^{18}O, respectively.
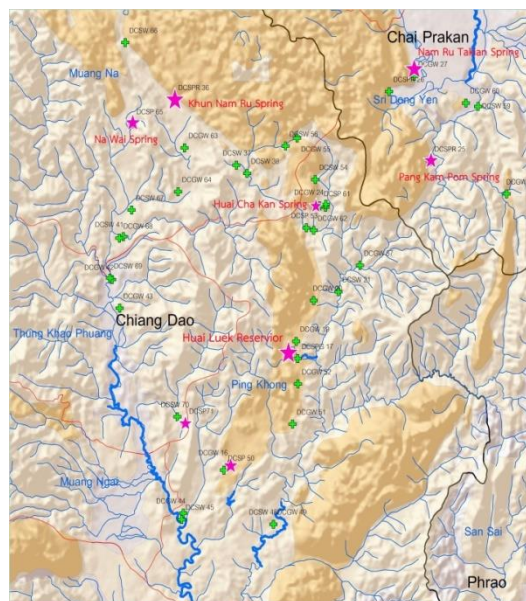

Figure 2 The location map showed the sampling locations of SW, GW (green cross) and the location of springs (stars), outlets of the conduit networks. Background colors showed the geological map of Permian Ngao Group (Orange), which was exposed as prominent exokarst at the high altitude, underlaid by Carboniferous-Permian metamorphic rocks of Mae Tha Group (light orange).
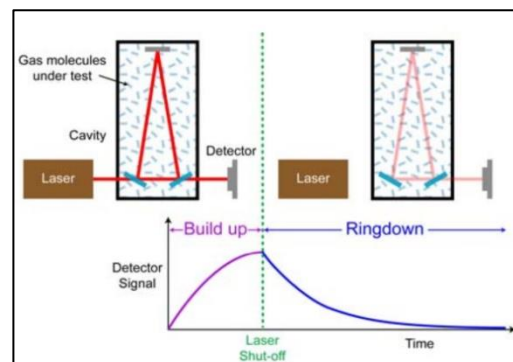

Figure 3 The isotopic H$_2$O analyzer Picarro L2130-*I* and schematic configuration of "CRDS" Spectrometry [9].

The radionuclide tritium content in water samples were analyzed by Liquid Scintillation Counter (LSC) with ultra-low level by electrolytic enrichment [10] (Figure 4).
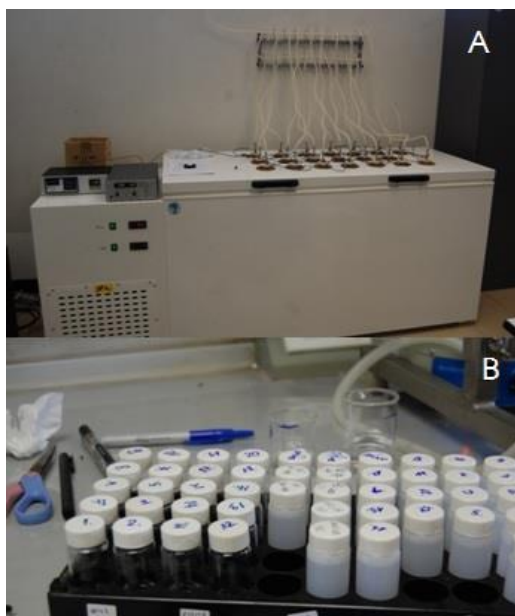

Figure 4 The ultra-low level tritium measurement by electrolytic enrichment (A) and LSC counting (B).

The samples were primary distilled to reduce impurities, which the conductivity are less than 30 µS/cm The primary distilled samples and 2 dead waters (Background tritium concentration) including 3 spike waters (known tritium concentration) in each 500 mL, were added 1.5 g of Na_2O_2 (analytical grade) and be enriched by electrolytic process. The electrolytic reduction was completed within 9 days; the 1st day was applied the current to 3.5 A, the 2nd was adjusted 7.0 A (Charge $\geq$ 84 Ah), the current at 10 A (Charge $\geq$ 252 Ah) was tuned in the 3rd day and held on to 6th day, then the 7th was decreased the current to 6.0 A (Charge $\geq$ 1212 Ah) and 3.3 A (Charge $\geq$ 1353 Ah) on 8th day, finally, this process was ended to 3.3 A (Charge $\geq$ 1423 Ah). Additionally, the enriched samples were distilled (secondary distillation) with 6 g of $PbCl_2$ (analytical grade) in each (pH $\leq$ 7.5). The secondary residues, each combination with 8 mL ($\approx$ 8 g) of water sample and 12 mL of scintillant (UltimaGold LLT, Perkin Elmer) was filled in polyethylene scintillation vial and 6 extra vials (2 spikes, 2 standards, and 2 dead waters) with same combination. All 26 samples were analyzed by liquid scintillation counter in the energy range of 0-18.6 keV by 50 min/cycle for 10 cycles. The

counting results will be calculated the tritium contents in Tritium Unit (TU) and uncertainty of measurements is ±0.1 to 0.4 TU.

Results and Discussion

The stable isotope data in water samples were evaluated by $\delta^2H/\delta^{18}O$ plots, which the stable isotope fingerprints of SW, GW and springs can be identified. They can be used for the interpretation of their sources and relationships in the local water system (Figure 5).

In SW, the recent isotope data show the local evaporation trend, which reservoir water can be separated to streams by very high enrichment ($\delta^{18}O$ >-5.0) fingerprints by repeat evaporation of less circulation characteristic. The fingerprint can be traced in the GW system and defined clearly SW-GW interaction by the criteria of $\delta^{18}O$ > -7.1, which found in 2 groundwater wells and 5 springs that located close to the reservoirs.
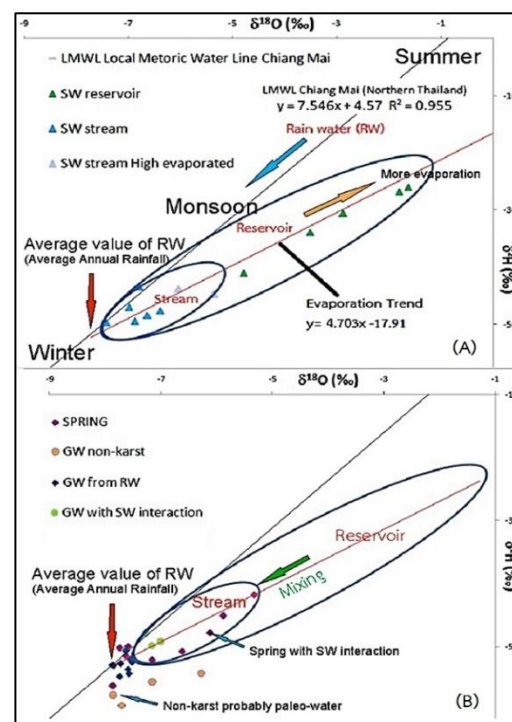

Figure 5 The $\delta^2H/\delta^{18}O$ plots show isotope fingerprints and interpretations on the surface water (A) GW and springs (B).

In contrast, almost GW and springs were measured -7.94< $\delta^{18}O$ <-7.10, which can be related to the average value of local rainfall (Chiang Mai) and position on the Local Meteoric Water Line (LMWL) [11], which can be interpreted as rain water

recharged origin. The interpretation of some selected GW and spring were shown in Table 1.

Table 1 Summary of GW and springs interpretation by the stable isotope fingerprints.

sample No.	Location	sample type	δ2H	δ18O	interpretation
DCGW 16	รร. บ้านปางเฟือง	GWB	-49.18	-7.01	GW with SW interaction
DCGW 23	รร.ห้วยฮอยต่าน	GWB	-47.81	-7.28	GW from the rain (Longer recharged)
DCSPR 25	น้ำรูบางขยามป้อม	Spring	-49.89	-7.59	Spring Recharded from RW
DCSPR 26	น้ำรูดอะเตียน	Spring	-51.43	-7.64	Spring Recharded from RW
DCSPR 36	จุนน้ำรู	Spring	-50.23	-7.75	Spring Recharded from RW
DCGW 42	รร.บ้านห้วยเป้า	GWB	-54.24	-6.28	GW old water non-karst
DCGW 43	รร.ทุ่งข้าวพวง	GWB	-55.60	-7.16	GW old water non-karst
DCGW 44	วัดป่งโค่ง	GWB	-59.35	-7.71	GW old water non-karst
DCSP 50	น้ำพุ บ.ปางเฟือง	Spring	-47.77	-6.12	Spring with SW interaction
DCGW 51	บ.ป่าง้ม	GWB	-57.71	-7.86	GW old water non-karst
DCGW 52	บ.ไทรสามัคคี	GWB	-54.66	-7.75	GW from the rain (Longer recharged)
DCSP 53	น้ำพุ บ.นาน้อย	Spring	-41.73	-5.33	Spring with SW interaction
DCSP 61	น้ำพุ บ้านห้วยจอะต่าน	Spring	-50.74	-6.63	Spring with SW interaction
DCGW 62	บ.สียอทรงงาน	GWB	-52.44	-7.52	GW from the rain (Longer recharged)
DCGW 64	บ.ท่าดินต่ำ	GWB	-53.01	-7.86	GW from the rain (Longer recharged)
DCSP 65	น้ำรู นาหวาย	Spring	-52.07	-7.16	Spring Recharded from RW
DCGW 68	วัดห้วยไส้	GWB	-53.52	-7.59	GW from the rain (Longer recharged)

Tritium contents in SW collected in the study area are ranged from 1.8-2.3 Tritium Unit (TU), which can be compared to the values in recently measured in the precipitations (collected in Ongkarak Nuclear Research Centre, Nakorn Nayok). The range can be used as defining values of "Modern water" tritium contents in local area.

Furthermore, tritium contents in GW and springs in recent study range from 0.3-2.0 TU, and can be divided into 2 groups by the range and the correlation the attitude (in above Mean Sea Level, MSL.) of sampling points (Figure 6).

First group, the GW in recharge area at higher altitude (>620 m above MSL.) were measured the tritium contents of 1.8-2.0 TU They can be interpreted as relation of modern water recharged (by rain water or SW). The second group is GW in discharge area at lower altitude (422-620 m above MSL.). They can be measured the tritium contents of 0.3-1.9 TU This group can be defined as mixture of younger recharged of modern water and the older saturated water in aquifers (below dry season GW water levels or base level), which characterized by background level tritium content of sub-modern (prior 1952) water.

Conclusions

The GW system including springs the study area can be separated into 2 groups by the altitude and their hydrological characteristics, reviewed by stable isotopes and tritium contents. In the recharged area (altitude >620 m), the water system are very dynamic responded to the sources of rain water and SW,

which show evaporation fingerprint and "Modern water" tritium characteristic. In contrast, the discharged area (altitude <620 m) the water system are less dynamic and not exhibited seasonal fluctuation by longer recharged mechanism and relative larger recharge area. The water system in higher altitude, which the important criterion of altitude about 620 m above MSL., will be assessed as higher risk in short of storage or decline of water level by leakage or rapidly migrate to the lower GW water system (base flow) in the dry season.
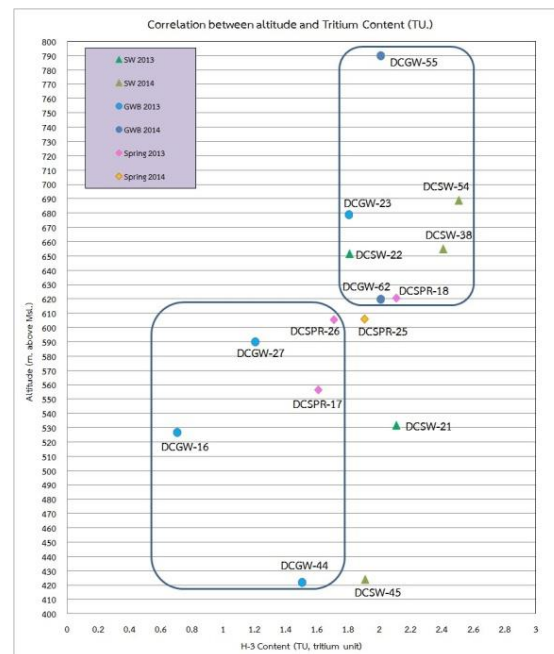

Figure 6 The relationship between the tritium content of water samples and altitudes (above MSL.)

Acknowledgments

References

[1] Bunopas, S. 1981. Paleogeographic history of western Thailand and adjacent parts of Southeast Asia a plate tectonics interpretation, Ph.D. Thesis, Victoria Univ. of Wellington, New Zealand, 810 p.

[2] Ford, D. C. and Williams, P. 2007. Karst hydrology and geomorphology, 562 p.

[3] Freeze A. R. and Cherry J.A. 1979. Groundwater, Prentice Hall Inc., 604 p.

[4] Mazor E. (ed.) 2004. Chemical and Isotopic Groundwater Hydrology, Marcel Dekker, Inc., New York, 453 p.

[5] Mook W. G. (ed.) 2000. Environmental Isotopes in the Hydrological Cycle vol. 1: Principles and Applications, IAEA, Vienna, 164 p.

[6] Coplen T.B. 1996. New reporting of stable hydrogen, carbon, and oxygen isotopic abundances. Geo.Cos.Act. 60: 3359-3360.

[7] Beer A. 1852. Bestimmung der Absorption des rothen Lichts in farbigen Flüssigkeiten. Annal. Phys. Chem 86: 78–88.

[8] O'Keefe A. and Deacon A.G. 1988. Cavity ring-down Optical Spectrometer for absorption measurements using pulsed laser sources. Review of Scientific Instruments 59: 2544-2551.

[9] Woelk M (Unpublished). Simple, Real-Time Measurement of Stable Isotope Ratios in H_2O and CO_2, Picarro Inc., Sunnyvale, Unpublished white paper, 6 p.

[10] Rozanski K. and Gröning M 1998. Tritium assay in water samples using electrolytic enrichment and liquid scintillation spectrometry. In Proceedings of a Consultants Meeting on Quantifying Uncertainty in Nuclear Analytical Measurements, IAEA, Vienna: 195-217.

[11] Thailand Institute of Nuclear Technology 2015 (Unpublished report in Thai). รายงานโครงการจัดทำฐานข้อมูลไอโซโทปเสถียรของความชื้นอากาศ น้ำฝน น้ำท่า เพื่อศึกษาวัฏจักรของน้ำในประเทศไทย, 672 หน้า.